








The Dynamics, Structure, and Fate of a Young Cluster during Gas Dispersal: Hectoschelle, *Chandra*, *Spitzer*, and *Gaia* Observations of Cep OB3b

N. Karnath¹, J. J. Prchlik² , R. A. Gutermuth³ , T. S. Allen^{4,5}, S. T. Megeath¹ , J. L. Pipher⁶ , S. Wolk² , and R. D. Jeffries⁷

¹Department of Physics and Astronomy, University of Toledo, Toledo, OH 43606, USA; nicole.karnath@rockets.utoledo.edu, s.megeath@utoledo.edu

²Harvard-Smithsonian Center for Astrophysics, 60 Garden St., Cambridge, MA 02138, USA

³Department of Astronomy, University of Massachusetts, Amherst, MA 01003, USA

⁴Portland State University 1825 SW Broadway Portland, OR 97207, USA

⁵Lowell Observatory, 1400 West Mars Hill Road, Flagstaff, AZ 86001, USA

⁶Department of Physics and Astronomy, University of Rochester, Rochester, NY 14627, USA

⁷Astrophysics Group, Keele University, Keele, Staffordshire ST5 5BG, UK

Received 2018 September 29; revised 2018 November 6; accepted 2018 November 9; published 2019 January 21

Abstract

We present a study of the kinematics and structure of the Cep OB3b cluster based on new spectra obtained with the Hectoschelle spectrograph on the MMT and data from *Spitzer*, *Chandra*, and *Gaia*. At a distance of 819 ± 16 pc, Cep OB3b is one of the closest examples of a young ($\sim 3\text{--}5$ Myr), large (~ 3000 total members) cluster at the late stages of gas dispersal. The cluster is broken into two subclusters surrounded by a lower density halo. We fit the empirical density law of King to each subcluster to constrain their sizes and structure. The richer eastern subcluster has circular symmetry, a modest central density, and lacks molecular gas toward its core, suggesting it has undergone expansion due to gas dispersal. In contrast, the western subcluster deviates from circular symmetry, has a smaller core size, and contains significant molecular gas near its core, suggesting that it is in an earlier phase of gas dispersal. We present posterior probability distributions for the velocity dispersions from the Hectoschelle spectra. The east will continue to expand and likely form a bound cluster with $\sim 35\%$ of stars remaining. The west is undergoing slower gas dispersal and will potentially form a bound cluster with $\sim 75\%$ of stars remaining. If the halo dissipates, this will leave two independent clusters with ~ 300 members; proper motions suggest that the two subcluster are not bound to each other.

Key words: open clusters and associations: Cep OB3b – stars: formation – stars: kinematics and dynamics – stars: pre-main sequence – techniques: radial velocities

1. Introduction

Most stars form in embedded clusters (Carpenter 2000; Lada & Lada 2003; Megeath et al. 2016), and within a few Myr, the natal gas will be expelled from the cluster, relieving it of internal extinction assuming dust moves with the gas. Given that star formation efficiency (SFE) is low, 4% for entire clouds and 20% in clusters (Lada & Lada 2003; Allen et al. 2007; Evans et al. 2009; Gutermuth et al. 2011b; Megeath et al. 2016), most of the mass leaves the cluster in a few Myr, drastically lowering the gravitational potential of the cluster. The ensuing dynamical evolution will determine whether the cluster—in whole or in part—will form a bound open cluster or disperse into the galactic disk. Cep OB3b is an excellent environment to study this crucial step of evolution because at $\sim 3\text{--}5$ Myr (Littlefair et al. 2010; Allen et al. 2012), the cluster has dispersed most of its natal gas and is observable at visible wavelengths. This gives a snapshot of cluster evolution toward the end of gas dispersal, in a birth cluster similar to that of the Sun (Adams et al. 2001), and at a later stage of evolution than the Orion Nebula Cluster (ONC).

Many numerical studies have been carried out to determine how clusters evolve during and after gas dispersal using a range of assumptions for the initial cluster properties and the timescale for gas dispersal (e.g., Lada et al. 1984; Adams 2000; Geyer & Burkert 2001; Boily & Kroupa 2003; Baumgardt & Kroupa 2007; Chen & Ko 2009; Goodwin 2009; Proszkow et al. 2009; Moeckel & Bate 2010; Pelupessy & Portegies Zwart 2012; Farias et al. 2015, 2018). Observational studies are limited at this crucial time during gas dispersal. Most of the

large, young clusters within 1 kpc, in particular Orion, NGC 2264, or Mon R2, are partially embedded and appear to be in earlier stages of their gas dispersal (Dahm & Simon 2005; Gutermuth et al. 2011b; Rapson et al. 2014). Comparisons of the number of embedded and bound clusters within ~ 2 kpc of the Sun indicate 7% of embedded clusters survive gas expulsion to form open clusters (Lada & Lada 2003). Determining the structure and kinematics of clusters undergoing gas dispersal is a key step toward improving our understanding of what factors determine whether a cluster survives.

Allen et al. (2012) carried out a census of the young stellar objects (YSOs) in Cep OB3b. They employed *Spitzer* data to identify stars with infrared excesses due to dusty disks or envelopes, a combination of new and archival *Chandra* data to detect X-ray emission from coronae of young stars, and visible light photometry from the literature to identify stars on the Cep OB3b isochrone. Allen et al. (2012) estimated that there are ~ 3000 total members in Cep OB3b consisting of primarily low-mass ($\leq 1 M_{\odot}$) stars. The density of stars is considerably less than the ONC (Hillenbrand & Hartmann 1998; Megeath et al. 2016), but it is comparable in size and membership to the ONC (Carpenter 2000; Allen et al. 2007), making Cep OB3b one of the largest known, young clusters within 1 kpc of the Sun (Allen et al. 2012). Most of the members, however, lie in a cavity of low extinction, implying that most of the natal gas has been dispersed. This combination of size and evolutionary state makes it an excellent region to study the effect of gas dispersal on young clusters. The spatial distribution of the objects shows

Table 1
Hectoschelle Observations

UT Date	R.A. (J2000)	Decl. (J2000)	Exposures (# × s)	Seeing (arcsec)	Airmass	# of Targets
2009 Oct 26	22 55 12.36	+62 40 11.64	4 × 1800	1.97	1.26	120
2009 Nov 03	22 55 09.12	+62 39 07.56	4 × 1800	1.76	1.23	123
2010 Nov 25	22 55 07.86	+62 42 16.02	4 × 1800	1.83	1.23	88
2011 Oct 20	22 55 08.04	+62 41 35.52	4 × 1800	0.72	1.25	153
2013 June 25	22 55 43.68	+62 39 03.24	4 × 2100	1.74	1.53	77

a hierarchical morphology composed of two distinct subclusters, denoted east (eastern subcluster) and west (western subcluster), each associated with a distinct molecular clump within the larger Cep OB3 molecular cloud (Sargent 1977; Heyer et al. 1996). Furthermore, a substantial difference in the disk fraction of the subclusters, $32\% \pm 4\%$ for the east and $50\% \pm 6\%$ for the west, was found by Allen et al. (2012) and was attributed to a difference in the typical ages of the constituent stars (east being older) in the subclusters, rather than the photoevaporation of disks by high-mass members. These results suggest a distinct origin for both subclusters; however, since the two subclusters share a contiguous region of high stellar surface density (Gutermuth et al. 2011a; Allen et al. 2012) within the Cep OB3b cloud with a diffuse halo of stars surrounding it, we consider these as parts of a single cluster. Cep OB3b has one O star (O7V, HD 217086) that resides in the eastern subcluster and several B stars throughout the entire cluster (Blaauw et al. 1959).

In order to relate young cluster populations to older stars in the field and open clusters, we need to observe young clusters at this critical stage of their evolution. The goal of this paper is to assess the kinetic and potential energy of the two subclusters, determine their fates as bound clusters, and study the effect of gas dispersal on young clusters. We carry out a radial velocity (RV) survey of 499 stars in Cep OB3b to measure the velocity dispersion and measure the kinetic energy. This study is complemented by an analysis of the structure of the two subclusters using *Spitzer* and *Chandra* data; from these data we can determine the current potential energy of the cluster. Prior to this study, the structure and kinematics of Cep OB3b have not been assessed using the population of low-mass stars. Finally, we use *Gaia* DR2 to both refine the distance to the cluster, which is needed to measure the potential energy of the cluster, and to measure the bulk motions of the subclusters.

Velocity dispersions of YSOs have been measured for a number of young clusters and molecular clouds probing their kinematical states. The ONC has been observed several times in RV surveys to determine velocity dispersions: $\sim 1.8 \text{ km s}^{-1}$ (Sicilia-Aguilar et al. 2005), $\sim 2.3 \text{ km s}^{-1}$ (Fűrész et al. 2008), $\sim 2.5 \text{ km s}^{-1}$ (Tobin et al. 2009), $\sim 2.3 \text{ km s}^{-1}$ (Kounkel et al. 2016), and $\sim 1.7 \text{ km s}^{-1}$ (Da Rio et al. 2017). Da Rio et al. (2014) found that the ONC is an expanding cluster undergoing gas expulsion, which is in agreement with Kuhn et al. (2018), who measured a parallax-based velocity dispersion from *Gaia* DR2 data of $\sim 1.8 \text{ km s}^{-1}$.

Outside of Orion, Hectoschelle observations of NGC 2264 by Fűrész et al. (2006) and Tobin et al. (2015) found a one-dimensional velocity dispersion of $\sim 2.5 \text{ km s}^{-1}$ and classified the region as several clumps of star formation and not as one bound cluster. NGC 1333 was studied with APOGEE, which measured a velocity dispersion of $\sim 1 \text{ km s}^{-1}$, yielding a

virialized cluster with some initial substructure (Foster et al. 2015). The APOGEE project also observed IC 348, measuring a velocity dispersion of $\sim 0.7 \text{ km s}^{-1}$ and implying a super-virial state; consistent with IC 348 being in an advanced phase of gas dispersal (Cottaar et al. 2015). Ortiz-León et al. (2018) used the *Gaia* DR2 release on IC 348 and NGC 1333 and found velocity dispersions that agree with the APOGEE project.

The *Gaia*-ESO survey studied several young regions, probing their kinematical structure: Jeffries et al. (2014) determined there were two kinematical populations in γ Vel B with velocity dispersions of 1.6 and 0.34 km s^{-1} , Rigliaco et al. (2016) determined a velocity dispersion of 1.14 km s^{-1} in L1688 in the ρ Ophiuchi molecular cloud, and Sacco et al. (2017) recorded a velocity dispersion of 1.1 km s^{-1} in Chamaeleon I. For post-gas-dispersal clusters, Jeffries et al. (2006) determined there are two spatially superimposed components in σ Ori with velocity dispersions of 1.1 and 1.3 km s^{-1} , and Kuhn et al. (2014) studied NGC 6231 in the Sco OB1 association and found it is gravitationally bound.

In Section 2, we describe our observations and data reduction. In Section 3, we provide our analysis, and Section 4 contains the results. We discuss implications of the results in Section 5 and summarize the paper in Section 6.

2. Hectoschelle Observations and Data Reduction

The spectra were obtained on the MMT with Hectoschelle (Szentgyorgyi et al. 1998), a fiber-fed, echelle spectrograph with a resolving power of $\sim 32,000$. The 240 fibers are robotically placed on the maximum possible number of target stars for a given configuration. Five epochs of observations were taken over five years (2009–2013; see Table 1) using the 25th order; these spectra span 150 \AA centered on $H\alpha$ at 6563 \AA . Every configuration had ~ 30 fibers placed on the sky to measure the sky emission, and the remaining fibers were placed on target stars with integration times of $4 \times 1800 \text{ s}$, except for the final epoch, which was $4 \times 2100 \text{ s}$. In addition, one set of spectra was obtained with the telescope offset by $5''$ from the target stars per configuration to measure the contribution of interstellar lines in the spectra.

The target stars are from the combined visible, infrared, and X-ray study of Allen et al. (2012). They determined membership by the detection of an IR excess with *Spitzer* IR using color–color diagrams, by the detection of X-ray emission from enhanced coronal activity using novel and archival *Chandra* data, and—less reliably—by their coincidence in V versus $V-I$ diagrams with the isochrone of members identified with the X-ray and *Spitzer* data. Diskless members with X-ray detections were the highest priority targets of the survey since $H\alpha$ emission dominates the spectrum of disk objects due to accretion. *Spitzer*-identified YSOs with disks, both Class II and

Table 2
2009.1026 RV Results

2MASS ID	R.A. (J2000)	Decl. (J2000)	RV $\pm \sigma$ (km s ⁻¹)	R Value
J22554779+6251042	22:55:47.76	62:51:04.39	-26.34 \pm 5.80	0.80
J22551448+6245480	22:55:14.47	62:45:47.96	-35.16 \pm 10.39	0.95
J22553253+6253096	22:55:32.52	62:53:09.48	-22.13 \pm 4.20	2.05
J22554968+6255229	22:55:49.70	62:55:22.88	-5.36 \pm 0.81	13.36
J22561275+6300232	22:56:12.75	63:00:23.22	-69.87 \pm 5.06	2.23
J22550645+6241517	22:55:06.47	62:41:51.78	15.38 \pm 2.54	4.43
J22564218+6255417	22:56:42.21	62:55:41.48	-4.43 \pm 1.03	10.47
J22564927+6255456	22:56:49.26	62:55:45.83	-0.27 \pm 0.83	13.06
J22562362+6256000	22:56:23.61	62:55:59.94	-8.39 \pm 4.80	1.50
J22563411+6256466	22:56:34.14	62:56:46.72	-0.43 \pm 1.43	7.00
J22555515+6250306	22:55:55.14	62:50:30.50	-29.83 \pm 6.01	1.16
J22560500+6248269	22:56:05.01	62:48:26.78	-19.76 \pm 2.34	4.57
J22555564+6244178	22:55:55.62	62:44:18.05	-11.26 \pm 1.09	9.57
J22563549+6250400	22:56:35.50	62:50:39.99	-29.51 \pm 1.29	8.76
J22560723+6245358	22:56:07.23	62:45:35.76	-15.69 \pm 6.15	2.18
J22552722+6243290	22:55:27.23	62:43:28.90	15.19 \pm 5.35	6.34
J22562018+6247045	22:56:20.19	62:47:04.59	-22.20 \pm 3.28	5.77
J22553606+6238563	22:55:36.25	62:39:02.35	-11.49 \pm 1.36	8.27
J22561571+6242509	22:56:15.72	62:42:51.08	-12.90 \pm 2.58	5.77
J22560574+6242599	22:56:05.75	62:42:59.74	6.90 \pm 2.84	2.24
J22561829+6245166	22:56:18.28	62:45:16.38	-25.06 \pm 6.21	3.30
J22570068+6245485	22:57:00.70	62:45:48.44	-20.45 \pm 10.68	3.06
J22584063+6250288	22:58:40.61	62:50:28.84	-12.25 \pm 2.44	3.06
J22563906+6245092	22:56:39.04	62:45:09.22	36.56 \pm 1.56	6.88
J22564077+6245453	22:56:40.74	62:45:45.36	-46.79 \pm 6.56	2.78
J22561377+6240505	22:56:13.76	62:40:50.60	-1.17 \pm 6.70	3.43
J22570209+6244070	22:57:02.07	62:44:07.21	-18.62 \pm 4.25	7.14
J22562637+6241289	22:56:26.37	62:41:28.94	-13.31 \pm 1.19	10.05
J22561535+6242268	22:56:15.33	62:42:27.04	-12.35 \pm 1.27	8.62
J22571960+6241559	22:57:19.56	62:41:55.61	-29.48 \pm 3.18	1.84
J22570858+6242536	22:57:08.60	62:42:53.53	-12.50 \pm 4.23	2.42
J22565527+6242240	22:56:55.27	62:42:24.15	-8.72 \pm 1.74	9.69
J22573867+6242246	22:57:38.68	62:42:24.71	-14.69 \pm 1.44	6.05
J22564486+6237541	22:56:44.88	62:37:53.99	-10.74 \pm 1.41	8.83
J22562890+6238411	22:56:28.91	62:38:41.25	-15.64 \pm 2.07	8.01
J22562723+6239197	22:56:27.22	62:39:19.80	-16.22 \pm 1.43	8.65
J22565186+6239521	22:56:51.86	62:39:51.96	-10.70 \pm 1.39	8.12
J22561749+6240116	22:56:17.49	62:40:11.71	-14.35 \pm 2.14	5.24
J22560527+6238379	22:56:05.29	62:38:38.06	-7.59 \pm 2.87	2.88
J22553095+6238300	22:55:30.93	62:38:30.23	-23.82 \pm 3.88	2.17
J22554154+6239030	22:55:41.54	62:39:03.11	-21.34 \pm 2.41	4.83
J22555010+6237443	22:55:50.12	62:37:44.52	-4.74 \pm 2.48	7.71
J22561343+6236452	22:56:13.41	62:36:45.51	-0.94 \pm 7.96	2.08
J22570919+6233337	22:57:09.25	62:33:33.59	7.32 \pm 8.98	3.53
J22561122+6233290	22:56:11.21	62:33:28.97	-18.22 \pm 6.17	1.14
J22565436+6231597	22:56:54.36	62:31:59.72	-8.92 \pm 0.97	12.03
J22562445+6233559	22:56:24.47	62:33:55.89	-32.36 \pm 4.10	1.65
J22563622+6231246	22:56:36.21	62:31:24.55	-16.06 \pm 4.01	4.60
J22554765+6236152	22:55:47.65	62:36:15.22	-11.63 \pm 1.78	5.37
J22562852+6232301	22:56:28.50	62:32:30.07	1.91 \pm 1.04	10.81
J22560177+6233119	22:56:01.77	62:33:11.84	-15.53 \pm 3.72	3.32
J22553370+6233093	22:55:33.70	62:33:09.21	-4.90 \pm 2.09	7.09
J22552541+6237286	22:55:25.40	62:37:28.52	-12.30 \pm 2.21	4.40
J22554507+6232447	22:55:45.04	62:32:44.64	-19.86 \pm 3.98	2.75
J22561943+6228096	22:56:19.43	62:28:09.67	-11.71 \pm 3.40	2.09
J22551496+6232382	22:55:14.96	62:32:38.30	-33.30 \pm 1.76	7.56
J22561778+6223378	22:56:17.79	62:23:37.70	-18.99 \pm 0.58	19.02
J22555063+6228416	22:55:50.61	62:28:41.52	-18.72 \pm 5.83	2.99
J22550523+6238000	22:55:05.20	62:38:00.14	-34.17 \pm 0.77	14.28
J22553247+6231367	22:55:32.42	62:31:36.71	-26.96 \pm 6.39	2.17
J22545686+6234128	22:54:56.86	62:34:12.58	-9.17 \pm 4.54	5.90
J22551243+6230162	22:55:12.43	62:30:16.16	-46.15 \pm 0.79	13.18
J22545903+6237177	22:54:59.03	62:37:17.82	-18.48 \pm 3.74	4.28
J22545665+6239375	22:54:56.67	62:39:37.58	-10.82 \pm 1.02	10.11

Table 2
(Continued)

2MASS ID	R.A. (J2000)	Decl. (J2000)	RV $\pm \sigma$ (km s ⁻¹)	R Value
J22545364+6234031	22:54:53.61	62:34:03.10	-18.92 \pm 3.57	5.32
J22543747+6225456	22:54:37.47	62:25:45.69	-31.61 \pm 7.49	0.84
J22543882+6223364	22:54:38.82	62:23:36.61	-11.39 \pm 0.79	13.85
J22545101+6239064	22:54:50.99	62:39:06.53	-22.20 \pm 8.00	1.32
J22533383+6223183	22:53:33.82	62:23:18.13	7.09 \pm 0.88	12.23
J22541607+6230398	22:54:16.07	62:30:39.76	-19.90 \pm 1.10	9.55
J22535527+6233218	22:53:55.26	62:33:21.76	-21.93 \pm 6.63	3.07
J22542077+6236223	22:54:20.75	62:36:22.42	51.74 \pm 1.61	7.51
J22542405+6235158	22:54:24.04	62:35:15.95	-1.88 \pm 4.77	5.65
J22530748+6225036	22:53:08.57	62:25:01.54	-21.95 \pm 7.81	1.59
J22544752+6240001	22:54:47.51	62:40:00.16	-25.52 \pm 1.33	7.80
J22523087+6231116	22:52:30.84	62:31:11.45	-13.52 \pm 6.06	1.67
J22541116+6235541	22:54:11.14	62:35:54.21	-10.40 \pm 1.62	6.04
J22534360+6235322	22:53:43.60	62:35:32.20	-38.99 \pm 6.97	2.37
J22540438+6235548	22:54:04.37	62:35:54.68	-11.81 \pm 5.33	4.45
J22532966+6234051	22:53:29.64	62:34:05.00	-21.55 \pm 2.02	7.15
J22540642+6236503	22:54:06.40	62:36:50.37	-4.72 \pm 0.97	11.11
J22532283+6237409	22:53:22.85	62:37:40.99	-6.43 \pm 3.43	3.67
J22530628+6236326	22:53:06.29	62:36:32.68	-28.86 \pm 5.59	1.17
J22535723+6236506	22:53:57.24	62:36:50.70	-58.37 \pm 2.02	6.13
J22531785+6234592	22:53:17.86	62:34:59.10	-21.64 \pm 6.49	3.00
J22533489+6237007	22:53:34.91	62:37:00.69	-7.12 \pm 2.14	4.89
J22540731+6238098	22:54:06.84	62:38:06.56	-54.22 \pm 3.43	8.78
J22524589+6234125	22:52:45.92	62:34:12.53	-18.73 \pm 4.46	2.39
J22533413+6238199	22:53:33.19	62:38:20.55	-28.19 \pm 4.50	3.10
J22534448+6239061	22:53:44.43	62:39:06.52	-49.20 \pm 3.43	9.93
J22541525+6239469	22:54:15.24	62:39:46.89	-3.27 \pm 6.10	0.71
J22523061+6238279	22:52:30.61	62:38:28.15	-18.59 \pm 1.05	10.39
J22530993+6239119	22:53:09.91	62:39:12.16	-0.36 \pm 1.26	8.88
J22541906+6241367	22:54:19.05	62:41:36.73	-29.24 \pm 1.38	9.13
J22522918+6241092	22:52:27.48	62:41:10.30	-38.69 \pm 4.28	1.62
J22525962+6243050	22:52:59.63	62:43:05.07	-25.75 \pm 0.64	16.8
J22541227+6241154	22:54:12.29	62:41:15.39	-13.02 \pm 4.89	1.08
J22534690+6241504	22:53:46.90	62:41:50.54	-92.68 \pm 5.74	2.01
J22522631+6242084	22:52:26.32	62:42:08.72	-1.17 \pm 0.64	16.89
J22540632+6243500	22:54:06.33	62:43:50.09	30.02 \pm 1.34	7.61
J22541162+6242285	22:54:11.63	62:42:28.55	-28.24 \pm 10.86	1.71
J22543623+6241336	22:54:36.23	62:41:33.81	-39.95 \pm 0.99	10.77
J22535500+6243412	22:53:55.12	62:43:36.89	-20.80 \pm 5.16	1.03
J22535114+6245149	22:53:51.12	62:45:14.91	-3.09 \pm 1.96	5.12
J22543280+6242318	22:54:32.80	62:42:31.86	-17.64 \pm 7.89	2.74
J22542135+6248095	22:54:21.35	62:48:09.36	-10.42 \pm 1.33	8.11
J22545080+6240485	22:54:50.80	62:40:48.55	-11.79 \pm 1.20	9.59
J22542553+6244554	22:54:25.55	62:44:55.54	-40.35 \pm 0.84	12.68
J22543071+6245323	22:54:30.71	62:45:32.30	-74.41 \pm 3.91	12.90
J22540791+6248393	22:54:07.86	62:48:39.48	19.68 \pm 1.15	9.78
J22541238+6250443	22:54:12.36	62:50:44.34	-11.25 \pm 3.81	0.93
J22542503+6249009	22:54:25.05	62:49:00.77	8.21 \pm 0.92	11.96
J22541185+6253136	22:54:11.88	62:53:13.51	0.22 \pm 4.40	4.48
J22550261+6251081	22:55:01.39	62:51:11.83	-27.97 \pm 3.78	5.39
J22542910+6254472	22:54:29.07	62:54:47.07	-24.82 \pm 5.42	1.87
J22545316+6250085	22:54:53.16	62:50:08.35	-25.52 \pm 4.63	2.34
J22543257+6257160	22:54:32.61	62:57:15.97	-35.62 \pm 8.34	1.12
J22552832+6254286	22:55:30.02	62:54:32.96	12.58 \pm 1.28	8.50
J22552191+6251339	22:55:21.17	62:51:26.51	-22.11 \pm 1.25	8.21
J22550699+6248278	22:55:06.98	62:48:27.96	-4.91 \pm 1.11	10.49

transition-disk objects, were given second priority. Third priority was assigned to the potential members identified in the V versus $V - I$ color–magnitude diagram; these would be diskless members without detectable X-ray measurements. The

lowest ranked objects were objects with a V -band magnitude of ~ 11.5 – 14.5 regardless of the potential for membership. These objects were targeted if no more fibers could be placed targeting any of the three higher ranked objects. A total of 561

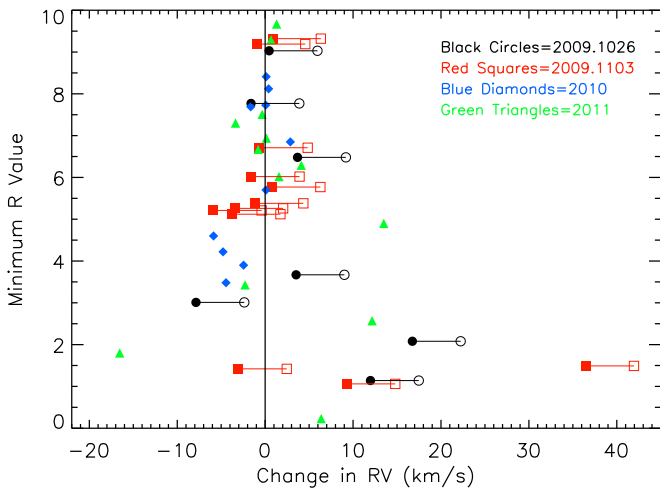


Figure 1. Minimum R value vs. change in RV for objects observed in two epochs. The x -axis is the difference in RV between the two epochs. This excludes objects that were flagged as binaries in the initial cross-correlation. The observations from 2009.1026/1103 (black circles/red squares, respectively) have a systematic non-zero change in RV compared to the 2010 (blue diamonds) and 2011 (green triangles) epochs at high R . The RV results from both 2009 epochs were shifted by an offset of 5.5 km s^{-1} ; the open symbols show the change in the RV, and the filled symbols connected to these by a line show the change after the offset was applied.

spectra (over five epochs; see Tables 2–6) were taken toward Cep OB3b of 499 distinct stars, 190 of which were identified as members using the above criteria.

All spectra were reduced following the procedure in Szentgyorgyi (2006), which uses the standard IRAF reduction pipeline for echelle spectra. Cep OB3b has a significant amount of nebular emission stemming from the S155 H II region nearby. Spectra of the nebulosity taken at offset positions were used to subtract out the contribution from the nebular emission, as described in J.J. Prchlik et al. (2019, in preparation).

3. Extraction of RVs

We used the *rvsao* package (Kurtz & Mink 1998) within IRAF to determine the RV of each spectrum. Synthetic spectral templates from Munari et al. (2005) were adopted for the cross-correlation. The templates had $[\text{Fe}/\text{H}] = +0.5$ solar using the stellar atmosphere models from Kurucz (1993) that covered 2500–10500 Å with a resolving power of 20,000. A supersolar metallicity was chosen to account for higher metallicity in younger stars compared to the Sun. Each spectrum was cross-correlated with 11 templates ranging from 3500 to 6250 K in steps of 250 K. We also cross-correlated with the higher resolution synthetic templates of Coelho et al. (2005). These provided solutions consistent with those using Munari et al., hence we adopted the RV values using the Munari et al. templates because they were closer in resolution to our data. The $\text{H}\alpha$ region (6559–6566 Å) was masked out of all spectra regardless of strength to avoid contamination of the extracted RV. We did not account for potential broadening of the lines by stellar rotation. Regions in the spectra with high nebular contamination were also masked out individually by eye to avoid contamination of the measured RV.

The best matching template (highest R value; Tonry & Davis 1979) was selected, yielding the RV and uncertainty used in this analysis. The R value corresponds to the quality of

the cross-correlation and scales as $R = h/\sqrt{2}\sigma_a$, where h is the height of the cross-correlation peak, and σ_a is the estimated uncertainty from the rms of the antisymmetric portion of the correlation function. An RV range of -50 to $+50 \text{ km s}^{-1}$ was used as an initial restriction. Each cross-correlation plot was inspected by eye. Some objects had a strong peak outside of this range. For these objects, the range was extended and run again, and the highest R value template result was adopted. Inspection by eye also enabled us to identify objects that were potential binaries. The RV values are given in Tables 2–7; all reported RVs are in terms of the local standard of rest, V_{lsr} .

The fifth epoch, 2013, observed 64 objects for a second time in addition to 13 objects not previously observed. This was useful to find binaries in the sample in addition to testing the consistency of the velocity calibration.

Figure 1 shows the difference in RV versus the minimum R value of 42 objects that were observed twice and were not initially suspected as binaries based on the shape of their cross-correlation plots (see Section 3.1). For 19 stars, we find a consistent offset between the 2009 epoch RVs compared to the 2013 measurement. This offset is not present when comparing the 2010 and 2011 RVs to the 2013 RVs for the 23 stars observed in those epochs.

In order to quantify the offset, we calculated a weighted average of the RV change between epochs with R of 6 or higher, yielding 5.5 km s^{-1} with an error on the mean of 0.19 km s^{-1} . Normally, a $\sim 5 \text{ km s}^{-1}$ difference between epochs would indicate a binary (assuming the uncertainties are less) since the offset is apparent in most of the sources with high R values. That is not the case for these specific objects. In contrast, for the objects that were originally observed in 2010 or 2011 and observed again in 2013, a weighted offset of 0.1 km s^{-1} was found, with an error on the mean of 0.1 km s^{-1} . This offset is easily within the uncertainties of the data, and therefore, no offset correction was needed for the 2010 and 2011 epochs. The 5.5 km s^{-1} offset was applied to both 2009 epochs and the uncertainty of the offset was combined in quadrature with the velocity uncertainties of each object in the 2009 data. These corrected values and the combined uncertainties are used in the tables and analysis.

The RV measurements of all observations are listed in Tables 2–6. The origin of this offset remains unclear. The uncertainties obtained from our analysis are consistent with previous results from Hectoschelle (Fűrész et al. 2006, 2008; Tobin et al. 2009, 2015; Kounkel et al. 2017).

3.1. Identifying Binaries

Potential spectroscopic binaries are listed in Table 7. Binaries of similar mass give a double-peak correlation plot, which was seen in 15 objects. For mass ratios less than unity, the primary component will dominate the spectrum and thus the RV will measure the motion of the primary. The secondary component may contaminate the spectrum enough to add an asymmetry. A total of 39 objects with significant asymmetries in their cross-correlation curves were also marked as potential binaries. If a source was observed twice, we compared the RVs to search for additional binaries. A shift in RV could be noticeable for short- to moderate-period binaries, i.e., orbital periods ranging from weeks up to ~ 10 yr. For objects with no companion, the RV should remain the same within the uncertainties. Of the 64 objects observed for a second time,

Table 3
2009.1103 RV Results

2MASS ID	R.A. (J2000)	Decl. (J2000)	RV $\pm \sigma$ (km s ⁻¹)	R Value
J22535500+6243412	22:53:55.00	62:43:41.24	-66.96 \pm 4.06	14.79
J22542631+6242377	22:54:26.33	62:42:37.77	-10.37 \pm 1.73	8.47
J22542993+6240335	22:54:29.92	62:40:33.57	-8.10 \pm 7.02	2.21
J22535448+6244536	22:53:54.47	62:44:53.72	-18.34 \pm 4.24	1.43
J22541764+6248194	22:54:17.64	62:48:19.40	-28.77 \pm 1.54	6.33
J22542450+6245330	22:54:24.51	62:45:32.96	-23.56 \pm 1.54	7.31
J22540417+6247032	22:54:04.16	62:47:03.23	-16.08 \pm 3.71	2.90
J22543463+6242480	22:54:34.62	62:42:47.99	-51.03 \pm 7.64	12.54
J22545800+6243449	22:54:58.03	62:43:44.95	-30.67 \pm 1.00	10.49
J22544726+6249150	22:54:47.28	62:49:15.14	0.19 \pm 6.30	2.02
J22543337+6256079	22:54:33.36	62:56:07.82	-25.93 \pm 11.50	1.78
J22541872+6251459	22:54:18.72	62:51:45.89	-11.51 \pm 3.50	0.67
J22543667+6249120	22:54:36.68	62:49:11.94	-3.71 \pm 4.39	7.03
J22543513+6245431	22:54:35.14	62:45:43.20	-39.69 \pm 7.02	2.54
J22542604+6255213	22:54:26.06	62:55:21.21	-13.39 \pm 1.06	9.74
J22551415+6255523	22:55:14.13	62:55:52.37	-36.43 \pm 0.77	14.45
J22550275+6241499	22:55:02.73	62:41:49.95	-18.19 \pm 4.34	1.64
J22550915+6253570	22:55:09.14	62:53:57.12	-31.49 \pm 7.90	3.86
J22550636+6256529	22:55:06.36	62:56:52.85	-27.91 \pm 1.54	7.06
J22553178+6246430	22:55:31.82	62:46:43.33	-22.70 \pm 0.89	11.93
J22554366+6250388	22:55:43.67	62:50:38.76	-10.54 \pm 2.18	3.46
J22552486+6246446	22:55:24.87	62:46:44.63	33.22 \pm 3.34	2.26
J22553847+6255182	22:55:38.46	62:55:18.17	-42.05 \pm 5.32	0.56
J22553242+6250527	22:55:32.39	62:50:52.65	-75.95 \pm 3.34	5.16
J22553628+6246094	22:55:36.27	62:46:09.56	-81.11 \pm 3.17	16.75
J22553545+6242343	22:55:35.44	62:42:34.38	-36.85 \pm 1.26	8.69
J22560150+6247467	22:56:01.48	62:47:46.73	-14.46 \pm 2.22	5.12
J22560924+6250324	22:56:09.98	62:50:13.96	12.32 \pm 3.88	0.94
J22560894+6251154	22:56:08.98	62:51:15.49	-11.26 \pm 1.15	9.01
J22562585+6253570	22:56:25.85	62:53:57.09	-51.51 \pm 3.38	9.36
J22561473+6247246	22:56:14.73	62:47:24.72	-12.46 \pm 1.54	6.40
J22564512+6246193	22:56:45.12	62:46:19.28	-12.09 \pm 1.66	6.74
J22560766+6246022	22:56:07.64	62:46:02.33	-9.63 \pm 4.18	0.94
J22562963+6245284	22:56:29.63	62:45:28.52	-10.77 \pm 1.55	9.45
J22570195+6251053	22:57:01.94	62:51:05.45	-34.10 \pm 0.67	15.18
J22563105+6246581	22:56:31.04	62:46:58.19	-13.48 \pm 1.04	10.82
J22554749+6241576	22:55:47.49	62:41:57.68	-11.94 \pm 4.73	3.12
J22573150+6243576	22:57:31.53	62:43:57.58	-15.16 \pm 2.26	3.80
J22564371+6242017	22:56:43.72	62:42:01.68	-12.56 \pm 5.08	3.12
J22562860+6244405	22:56:28.57	62:44:40.49	-11.17 \pm 1.63	6.46
J22563590+6242057	22:56:35.89	62:42:05.52	29.80 \pm 3.53	2.96
J22560428+6242388	22:56:04.27	62:42:38.89	26.53 \pm 12.40	2.19
J22565123+6243197	22:56:51.24	62:43:19.74	-18.12 \pm 2.77	5.80
J22561518+6242475	22:56:15.14	62:42:47.35	-12.90 \pm 2.01	4.30
J22562819+6242463	22:56:28.19	62:42:46.32	-32.09 \pm 1.22	7.96
J22564619+6244225	22:56:46.17	62:44:22.73	-14.92 \pm 1.77	5.77
J22570594+6238180	22:57:05.95	62:38:18.05	-13.51 \pm 2.08	5.52
J22562231+6240488	22:56:22.31	62:40:48.92	-10.51 \pm 1.65	6.71
J22570529+6238332	22:57:05.18	62:38:38.57	-39.06 \pm 1.15	8.38
J22563259+6238417	22:56:32.57	62:38:41.71	-26.41 \pm 14.55	0.68
J22560480+6239460	22:56:04.81	62:39:46.22	-10.67 \pm 1.08	9.19
J22563527+6239074	22:56:35.28	62:39:07.57	-12.91 \pm 2.21	5.21
J22563654+6240077	22:56:36.55	62:40:07.52	-61.53 \pm 4.64	7.45
J22562780+6239282	22:56:27.82	62:39:28.24	36.37 \pm 29.47	2.43
J22564296+6235316	22:56:42.94	62:35:31.62	-17.21 \pm 3.30	1.62
J22571485+6237437	22:57:14.85	62:37:43.82	-5.85 \pm 0.95	10.78
J22572343+6235141	22:57:23.43	62:35:14.10	-8.71 \pm 2.86	3.37
J22563865+6237140	22:56:38.68	62:37:14.29	-31.93 \pm 4.53	3.83
J22564210+6236207	22:56:42.11	62:36:20.88	-19.76 \pm 1.90	5.26
J22560823+6237034	22:56:08.23	62:37:03.54	-32.23 \pm 1.26	10.12
J22571812+6237011	22:57:18.13	62:37:00.98	-26.21 \pm 1.25	8.60
J22570709+6230189	22:57:07.08	62:30:19.05	-21.59 \pm 2.85	3.84
J22560306+6235187	22:56:03.04	62:35:18.71	-24.33 \pm 4.23	1.88
J22553832+6235472	22:55:38.32	62:35:47.31	3.00 \pm 0.19	...
J22562274+6232501	22:56:22.76	62:32:50.11	-16.13 \pm 8.07	1.54

Table 3
(Continued)

2MASS ID	R.A. (J2000)	Decl. (J2000)	RV $\pm \sigma$ (km s ⁻¹)	R Value
J22555686+6234332	22:55:56.85	62:34:33.24	-12.89 \pm 2.72	5.42
J22565217+6226391	22:56:52.17	62:26:39.06	2.97 \pm 0.19	...
J22570845+6225441	22:57:08.44	62:25:44.28	2.96 \pm 0.19	...
J22565569+6229183	22:56:55.67	62:29:18.36	2.97 \pm 0.19	...
J22563710+6229456	22:56:37.40	62:29:46.40	33.69 \pm 1.38	7.01
J22571116+6227330	22:57:11.15	62:27:33.00	43.02 \pm 9.30	1.03
J22562181+6223029	22:56:21.84	62:23:02.95	-12.96 \pm 0.85	12.99
J22553297+6233412	22:55:32.96	62:33:41.27	3.01 \pm 0.19	...
J22552589+6232538	22:55:25.89	62:32:53.85	-4.86 \pm 1.58	6.67
J22551567+6235261	22:55:15.67	62:35:26.16	-5.71 \pm 11.37	1.96
J22545580+6236233	22:54:55.94	62:36:23.34	3.02 \pm 0.19	...
J22560310+6225197	22:56:03.12	62:25:19.82	5.53 \pm 1.68	6.99
J22555006+6223083	22:55:50.15	62:23:08.25	-16.35 \pm 4.04	5.42
J22551657+6232522	22:55:16.59	62:32:52.12	-14.09 \pm 3.57	3.02
J22550265+6229136	22:55:02.64	62:29:13.61	-1.85 \pm 6.28	1.16
J22551869+6223517	22:55:18.70	62:23:51.79	-82.85 \pm 5.58	15.92
J22544780+6228506	22:54:47.81	62:28:50.46	34.37 \pm 5.48	0.98
J22545480+6233514	22:54:55.12	62:33:40.13	-27.72 \pm 1.32	7.47
J22545176+6230337	22:54:51.76	62:30:33.50	-43.55 \pm 1.52	6.38
J22544036+6233335	22:54:40.36	62:33:33.45	-9.52 \pm 1.04	9.89
J22544382+6230376	22:54:43.81	62:30:37.83	3.03 \pm 0.19	...
J22542760+6225270	22:54:27.60	62:25:26.87	-2.58 \pm 3.83	3.13
J22540555+6223064	22:54:05.54	62:23:06.65	-29.98 \pm 1.08	10.04
J22542257+6225041	22:54:22.56	62:25:04.02	-12.37 \pm 3.43	4.60
J22541824+6226460	22:54:18.24	62:26:45.93	-5.13 \pm 8.07	1.31
J22544224+6235548	22:54:42.23	62:35:54.93	-9.86 \pm 1.97	5.38
J22544431+6235183	22:54:44.31	62:35:18.23	10.50 \pm 0.96	11.75
J22542545+6234245	22:54:25.47	62:34:24.59	-14.97 \pm 1.41	8.12
J22530590+6225392	22:53:05.90	62:25:39.02	-22.23 \pm 0.76	14.61
J22522558+6222059	22:52:25.60	62:22:05.91	-14.94 \pm 6.56	2.64
J22531582+6230219	22:53:15.81	62:30:22.14	17.50 \pm 1.36	7.28
J22530014+6230588	22:53:01.67	62:30:55.69	4.78 \pm 0.94	10.75
J22525242+6228599	22:52:52.45	62:28:59.95	-3.58 \pm 4.95	2.18
J22543423+6235555	22:54:34.20	62:35:55.46	2.70 \pm 5.57	3.04
J22535395+6234504	22:53:53.93	62:34:50.29	-12.78 \pm 2.69	2.19
J22540214+6236278	22:54:02.16	62:36:27.78	-18.07 \pm 4.50	2.86
J22540337+6235322	22:54:03.39	62:35:32.25	-73.14 \pm 3.68	15.91
J22531578+6235262	22:53:15.78	62:35:26.13	-12.71 \pm 15.25	2.30
J22521616+6233017	22:52:16.16	62:33:01.65	-13.49 \pm 1.79	7.34
J22532187+6234490	22:53:21.86	62:34:48.95	-13.34 \pm 4.93	1.06
J22525910+6239184	22:52:59.12	62:39:18.55	1.37 \pm 0.93	11.58
J22533664+6236489	22:53:36.65	62:36:48.99	-13.82 \pm 7.32	3.85
J22523061+6238279	22:52:33.08	62:38:48.02	-71.28 \pm 4.49	17.09
J22533869+6237171	22:53:38.67	62:37:17.23	11.21 \pm 7.64	2.31
J22534042+6237564	22:53:40.40	62:37:56.44	3.57 \pm 2.10	4.03
J22532277+6237340	22:53:22.77	62:37:34.07	-11.14 \pm 1.88	5.31
J22524772+6240044	22:52:47.70	62:40:04.72	-16.89 \pm 3.81	2.85
J22544247+6237542	22:54:42.44	62:37:54.36	-18.86 \pm 9.65	1.21
J22522353+6244227	22:52:23.53	62:44:22.62	-44.65 \pm 0.93	11.60
J22525120+6241051	22:52:51.21	62:41:05.14	40.79 \pm 3.43	1.97
J22533793+6240148	22:53:37.94	62:40:14.86	-7.04 \pm 1.01	10.77
J22540382+6238211	22:54:03.84	62:38:21.03	-12.27 \pm 1.15	9.32
J22541076+6241389	22:54:10.75	62:41:38.90	-2.02 \pm 4.62	1.93
J22525607+6244047	22:52:56.06	62:44:04.73	-4.92 \pm 7.85	1.53
J22533684+6243149	22:53:36.83	62:43:14.88	-43.15 \pm 1.64	5.90
J22525172+6244534	22:52:50.98	62:44:46.91	32.27 \pm 5.91	0.72
J22540533+6240313	22:54:05.31	62:40:31.33	-14.72 \pm 6.10	1.18
J22534960+6241093	22:53:49.58	62:41:09.42	-11.89 \pm 4.60	1.17

34 disagree at the $>1\sigma$ level and 21 disagree at the $>2\sigma$ level. It is expected that at least 20 objects would differ at the 1σ level even if none are binaries; the larger number of objects in

disagreement suggests a short-period binary frequency of $\sim 20\%$ in our sample. We identify all of the $>1\sigma$ objects as potential binaries.

Table 4
2010 RV Results

2MASS ID	R.A. (J2000)	Decl. (J2000)	RV $\pm \sigma$ (km s ⁻¹)	R Value
J22542652+6247077	22:54:26.50	62:47:07.79	39.49 \pm 5.24	0.99
J22543806+6251022	22:54:38.06	62:51:02.27	-38.54 \pm 1.13	9.35
J22542386+6255382	22:54:22.92	62:55:24.16	40.46 \pm 3.22	1.65
J22543139+6251547	22:54:31.39	62:51:54.54	4.47 \pm 2.09	4.50
J22542604+6255213	22:54:27.90	62:55:26.17	50.14 \pm 4.53	1.77
J22545426+6254405	22:54:54.24	62:54:40.48	-105.70 \pm 0.73	14.22
J22551602+6255125	22:55:15.89	62:55:21.30	-36.91 \pm 4.06	1.85
J22550634+6253203	22:55:06.26	62:53:20.52	-39.92 \pm 1.46	6.96
J22550859+6255151	22:55:07.83	62:55:21.52	-41.43 \pm 3.21	1.92
J22550760+6244452	22:55:08.12	62:44:57.93	35.31 \pm 2.45	3.53
J22552454+6254456	22:55:24.52	62:54:45.70	-9.71 \pm 1.53	6.16
J22553086+6252057	22:55:30.86	62:52:05.64	-33.64 \pm 0.73	14.69
J22553847+6255182	22:55:37.59	62:55:19.18	49.39 \pm 7.66	1.06
J22553359+6253287	22:55:33.59	62:53:28.89	-12.82 \pm 1.54	6.38
J22555591+6252385	22:55:55.86	62:52:38.46	-15.80 \pm 7.92	2.22
J22561016+6249328	22:56:10.18	62:49:32.87	-21.10 \pm 5.64	1.60
J22562031+6254458	22:56:20.39	62:54:46.05	-17.91 \pm 1.62	7.73
J22571752+6256356	22:57:17.52	62:56:35.50	-51.19 \pm 1.15	9.13
J22562450+6254314	22:56:24.50	62:54:31.45	33.18 \pm 1.27	8.09
J22550959+6244210	22:55:09.61	62:44:21.04	-7.00 \pm 4.12	5.29
J22551755+6245458	22:55:17.53	62:45:45.94	-6.07 \pm 3.64	5.28
J22555228+6249200	22:55:52.27	62:49:20.03	-6.01 \pm 1.21	8.12
J22560030+6245029	22:56:00.31	62:45:03.05	-11.82 \pm 0.91	11.57
J22545157+6241522	22:54:51.54	62:41:52.35	-43.61 \pm 0.89	11.97
J22565619+6248492	22:56:56.22	62:48:49.24	-37.19 \pm 0.65	16.50
J22564191+6250549	22:56:41.91	62:50:54.96	23.15 \pm 7.62	0.74
J22560068+6245310	22:56:00.68	62:45:30.95	-9.33 \pm 1.59	5.70
J22551760+6243231	22:55:17.61	62:43:22.99	-9.33 \pm 2.84	6.56
J22561978+6248022	22:56:19.81	62:48:02.17	-2.35 \pm 3.75	3.78
J22563678+6246031	22:56:36.82	62:46:02.94	-8.02 \pm 7.08	3.83
J22572663+6243491	22:57:26.64	62:43:49.15	-14.69 \pm 1.06	11.05
J22560391+6243359	22:56:03.89	62:43:35.96	-11.12 \pm 1.18	8.41
J22562634+6242414	22:56:26.32	62:42:41.44	-13.29 \pm 1.32	10.39
J22565515+6245088	22:56:55.15	62:45:08.83	-12.75 \pm 3.35	4.05
J22561924+6242528	22:56:19.22	62:42:52.66	-4.74 \pm 1.08	9.48
J22570981+6245125	22:57:06.71	62:45:08.09	-66.04 \pm 0.82	11.73
J22562134+6243257	22:56:21.33	62:43:25.71	-12.87 \pm 3.89	6.73
J22583320+6247456	22:58:33.21	62:47:45.65	-9.05 \pm 14.90	1.69
J22555158+6239116	22:55:51.55	62:39:11.78	-8.56 \pm 1.04	10.55
J22565035+6242485	22:56:50.36	62:42:48.58	-15.15 \pm 4.60	1.87
J22570584+6239222	22:57:06.00	62:39:26.19	-32.25 \pm 0.92	11.69
J22570134+6242133	22:57:01.36	62:42:13.43	-12.87 \pm 13.56	2.14
J22561018+6239418	22:56:10.18	62:39:41.82	-10.93 \pm 3.73	2.29
J22551119+6239142	22:55:11.99	62:40:37.34	-11.25 \pm 1.47	6.50
J22555016+6240070	22:55:50.17	62:40:07.24	-9.27 \pm 0.99	12.59
J22563127+6240588	22:56:31.26	62:40:58.71	-11.92 \pm 4.30	3.89
J22554485+6237199	22:55:44.84	62:37:19.82	-10.05 \pm 14.08	0.94
J22564720+6237055	22:56:47.20	62:37:05.34	-10.26 \pm 3.57	4.22
J22560969+6237289	22:56:09.69	62:37:29.05	-16.30 \pm 6.33	0.54
J22544942+6239227	22:54:49.40	62:39:22.60	-9.59 \pm 1.55	6.85
J22560648+6234430	22:56:06.49	62:34:43.15	-30.00 \pm 1.06	10.11
J22565314+6232094	22:56:53.15	62:32:09.41	21.28 \pm 1.02	10.89
J22560790+6230425	22:56:07.90	62:30:42.56	-12.82 \pm 2.54	3.90
J22560767+6221482	22:56:07.72	62:21:48.07	-21.15 \pm 4.92	1.45
J22545509+6234545	22:54:55.07	62:34:54.41	25.39 \pm 15.02	1.34
J22544057+6238097	22:54:40.54	62:38:09.59	-3.91 \pm 6.45	1.38
J22542460+6225053	22:54:24.63	62:25:05:22	-25.93 \pm 1.95	5.08
J22543310+6233339	22:54:33.11	62:33:33.84	5.68 \pm 2.11	4.98
J22543924+6233469	22:54:39.25	62:33:46.79	-9.21 \pm 6.29	0.62
J22543166+6237117	22:54:31.65	62:37:11.78	-10.61 \pm 2.60	3.48
J22525674+6223004	22:52:56.72	62:23:00.49	-0.22 \pm 1.46	7.16
J22542236+6236471	22:54:22.35	62:36:47.25	-69.99 \pm 0.91	10.54
J22541270+6235379	22:54:12.70	62:35:37.89	-40.86 \pm 2.86	3.02
J22535945+6235102	22:53:59.42	62:35:10.21	53.78 \pm 3.16	2.10

Table 4
(Continued)

2MASS ID	R.A. (J2000)	Decl. (J2000)	RV $\pm \sigma$ (km s ⁻¹)	R Value
J22535969+6236320	22:53:59.69	62:36:32.03	-22.27 \pm 4.59	4.66
J22523376+6224147	22:52:33.75	62:24:14.71	0.55 \pm 1.96	5.24
J22534194+6234103	22:53:43.50	62:34:17.49	-44.68 \pm 0.69	15.29
J22535011+6234322	22:53:50.10	62:34:32.30	44.35 \pm 8.66	0.74
J22540194+6238255	22:54:01.92	62:38:25.45	-7.61 \pm 2.58	2.85
J22525102+6230436	22:52:51.00	62:30:43.51	3.00 \pm 1.33	7.63
J22531574+6234357	22:53:15.71	62:34:35.77	-41.03 \pm 3.84	2.79
J22524793+6230571	22:52:47.92	62:30:57.18	10.12 \pm 1.71	6.00
J22542708+6238531	22:54:27.07	62:38:53.06	-26.34 \pm 5.11	1.27
J22531015+6236444	22:53:10.17	62:36:44.41	-17.44 \pm 3.09	4.60
J22504792+6233227	22:50:47.94	62:33:22.62	-33.24 \pm 2.58	4.14
J22530436+6237249	22:53:04.38	62:37:24.91	-7.69 \pm 4.63	1.93
J22532653+6240134	22:53:26.53	62:40:13.57	-8.45 \pm 1.42	7.73
J22531297+6238444	22:53:12.99	62:38:44.39	-31.07 \pm 1.50	7.34
J02530517+6239073	22:53:05.03	62:39:09.61	-21.69 \pm 5.38	2.34
J22523412+6241513	22:52:34.10	62:41:51.26	-26.78 \pm 1.03	10.76
J22530099+6243548	22:53:01.01	62:43:54.70	-19.18 \pm 6.82	2.97
J22535397+6240249	22:53:53.95	62:40:24.90	-80.14 \pm 1.28	8.08
J22523028+6243087	22:52:30.31	62:43:08.63	42.75 \pm 1.79	0.03
J22532070+6242187	22:53:20.70	62:42:18.83	-11.24 \pm 3.06	5.50
J22533875+6242433	22:53:38.74	62:42:43.40	-4.59 \pm 0.83	12.78
J22540370+6242122	22:54:03.68	62:42:12.35	-19.16 \pm 9.52	1.01
J22540822+6243038	22:54:08.23	62:43:03.82	-42.74 \pm 2.49	3.70
J22541822+6245397	22:54:18.23	62:45:39.83	-117.54 \pm 0.99	10.04

3.2. The RV Analysis Sample

To reliably measure the velocity structure and dispersion of the Cep OB3b subclusters, we make three cuts to the RV data to ensure the reliability of the velocities. The first cut eliminates potential binaries as indicated in Section 3.1 (see Table 7). This cut reduces the sample from 190 to 109. The second cut utilizes the R value from *rvsao*, which is a measure of the signal-to-noise ratio. We reject objects that have an $R < 5$ (Figure 2). The value adopted for this cut comes from an analysis of the threshold R value versus the cumulative velocity dispersion, which examined the trade-off between sample sizes and the uncertainties in the RVs. In this analysis, the velocity dispersion was calculated for all the non-binary members at or below the R value of the bin (Figure 2). We adopted the threshold for R , which gave the minimum velocity dispersion for a sample size exceeding 30 objects; this minimum occurred at $R \sim 5$. Increasing the threshold reduces the number of objects, leading to fluctuations from small numbers statistics. A lower threshold includes objects with poorly constrained RV values with inherently large uncertainties associated. This cut reduces the sample from 109 to 62. The third cut is 3σ clipping from the average velocity of the 62 remaining members in the cluster to reduce the contamination by nonmembers. The cut leaves 57 objects remaining.

4. Results

In the following section, we focus on the properties of the two subclusters. The rationale for this approach is based on two observations. First, while the overall cluster is highly elongated and hierarchical in structure, each of the two subclusters has a single, centrally condensed core, and is much closer to circular symmetry (Figure 4 in Allen et al. 2012). This suggests that these are two distinct components within the larger cluster that

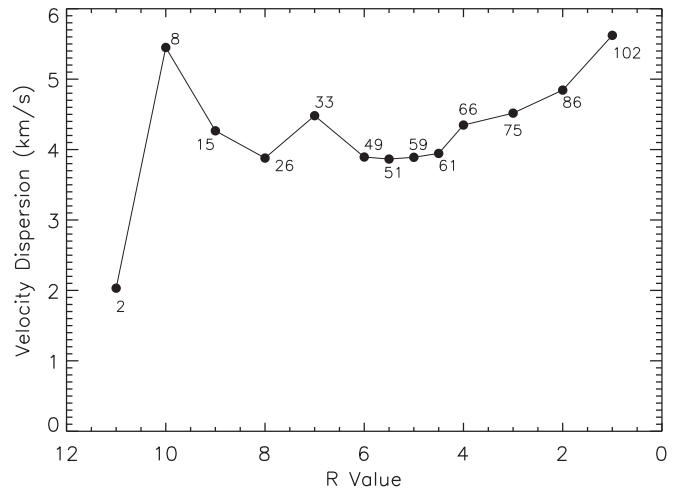


Figure 2. The velocity dispersion vs. minimum R value of the stars with youth indicators, which are not identified as binaries. The number of objects included in the calculation is next to each R value point. The velocity dispersion has a broad minimum around $R \sim 5$, which is adopted as the R cutoff in Section 3.2.

can be studied independently. Furthermore, each subcluster is associated with a distinct molecular clump within the larger parental clouds (Figure 4 in Allen et al. 2012). After using RVs to assess membership, we first characterize the structure of the two subclusters, fitting them to the empirical King (1962) model to constrain their three-dimensional structure. We then analyze the RV structure and velocity dispersion of each subcluster. Finally, we use *Gaia* DR2 to determine the distance of Cep OB3b and the bulk proper motions of the subclusters. From these results, we can also estimate the gravitational potential energy of the subclusters. These properties will

Table 5
2011 RV Results

2MASS ID	R.A. (J2000)	Decl. (J2000)	RV $\pm \sigma$ (km s ⁻¹)	R Value
J22544381+6243128	22:54:43.83	62:43:12.75	-31.44 \pm 2.01	4.81
J22535448+6244536	22:53:54.47	62:44:53.72	44.65 \pm 4.18	1.05
J22542553+6244554	22:54:25.56	62:44:55.54	-39.75 \pm 1.16	8.70
J22543560+6246312	22:54:35.59	62:46:31.16	9.57 \pm 4.79	2.31
J22545800+6243449	22:54:58.03	62:43:44.95	-30.83 \pm 1.43	6.59
J22544253+6245173	22:54:42.52	62:45:17.37	-75.62 \pm 0.85	11.72
J22541822+6245397	22:54:18.24	62:45:39.83	-121.27 \pm 0.70	14.38
J22543123+6245142	22:54:31.25	62:45:14.10	-57.97 \pm 0.68	14.66
J22542135+6248095	22:54:21.35	62:48:09.36	-9.31 \pm 1.12	9.15
J22545277+6246367	22:54:52.76	62:46:36.93	-23.24 \pm 6.97	1.85
J22550561+6244055	22:55:05.59	62:44:05.52	-27.65 \pm 13.85	1.67
J22542604+6255213	22:54:26.06	62:55:21.22	-13.34 \pm 1.19	8.31
J22543806+6251022	22:54:38.07	62:51:02.27	-37.44 \pm 0.74	13.86
J22543128+6251104	22:54:31.28	62:51:10.32	-1.78 \pm 3.39	4.65
J22542299+6251039	22:54:23.02	62:51:03.80	-18.08 \pm 18.35	2.31
J22541426+6254031	22:54:14.30	62:54:03.14	-39.64 \pm 1.52	8.38
J22543667+6249120	22:54:36.69	62:49:11.94	-59.90 \pm 1.15	10.34
J22545297+6257070	22:54:52.97	62:57:06.98	-30.78 \pm 0.59	17.47
J22544726+6249150	22:54:47.28	62:49:15.14	-3.62 \pm 9.37	2.03
J22550150+6245130	22:55:01.50	62:45:13.20	-61.67 \pm 1.09	9.47
J22544094+6254169	22:54:40.96	62:54:16.86	-104.43 \pm 0.49	21.14
J22545426+6254405	22:54:54.24	62:54:40.48	-105.19 \pm 0.54	18.95
J22550804+6244252	22:55:08.05	62:44:25.41	-5.57 \pm 1.83	8.61
J22551648+6250278	22:55:16.48	62:50:27.79	-38.49 \pm 0.63	16.58
J22551475+6256151	22:55:14.77	62:56:15.06	-83.59 \pm 0.70	14.67
J22550270+6249561	22:55:02.73	62:49:56.18	-24.35 \pm 0.96	11.37
J22550699+6248278	22:55:06.99	62:48:27.96	-4.54 \pm 1.25	9.25
J22550543+6256090	22:55:05.43	62:56:08.90	-8.85 \pm 1.40	7.48
J22551246+6251268	22:55:12.50	62:51:26.65	-21.77 \pm 1.96	4.96
J22552456+6255516	22:55:24.59	62:55:51.57	-77.58 \pm 0.99	10.74
J22552154+6252561	22:55:21.51	62:52:56.16	-23.65 \pm 5.80	0.96
J22552191+6251339	22:55:21.17	62:51:26.51	-21.39 \pm 1.25	8.41
J22551559+6244263	22:55:15.59	62:44:26.27	-28.56 \pm 0.67	15.85
J22552235+6250209	22:55:22.32	62:50:20.49	-2.14 \pm 0.81	11.45
J22551829+6246369	22:55:18.30	62:46:37.00	-7.95 \pm 0.91	11.82
J22552966+6251511	22:55:29.68	62:51:51.10	-39.32 \pm 1.07	9.40
J22563443+6256189	22:56:34.44	62:56:18.94	-29.57 \pm 0.59	17.62
J22551760+6243231	22:55:17.62	62:43:22.99	-10.32 \pm 2.57	7.24
J22553931+6251006	22:55:39.32	62:51:00.64	-6.83 \pm 1.54	6.74
J22553348+6246241	22:55:31.82	62:46:43.33	-22.02 \pm 0.85	12.70
J22554785+6252037	22:55:47.84	62:52:03.65	-13.88 \pm 7.14	3.32
J22554849+6250298	22:55:48.50	62:50:29.81	-79.84 \pm 1.27	7.51
J22563239+6250214	22:56:32.40	62:50:21.45	-37.40 \pm 2.79	4.75
J22561969+6253030	22:56:19.70	62:53:03.15	0.47 \pm 2.55	3.60
J22560500+6248269	22:56:05.02	62:48:26.79	-17.79 \pm 1.99	5.57
J22560167+6250058	22:56:01.66	62:50:05.83	-5.19 \pm 1.75	5.26
J22561016+6249328	22:56:10.19	62:49:32.87	-24.22 \pm 6.05	1.94
J22564968+6255018	22:56:49.68	62:55:01.80	-35.14 \pm 2.19	4.49
J22560998+6250140	22:56:09.99	62:50:13.96	-26.62 \pm 6.34	1.51
J22565588+625095	22:56:55.90	62:55:09.67	-19.10 \pm 3.93	1.47
J22555192+6244588	22:55:51.94	62:44:58.79	-75.56 \pm 0.75	14.27
J22570096+6252271	22:57:00.95	62:52:27.09	-29.46 \pm 0.66	15.64
J22565611+6249007	22:56:56.14	62:49:00.52	-5.76 \pm 0.99	9.95
J22553580+6245095	22:55:35.85	62:45:09.50	-22.20 \pm 13.47	1.01
J22555107+6245182	22:55:50.23	62:45:24.68	-28.66 \pm 6.66	1.68
J22561978+6248022	22:56:19.81	62:48:02.17	-13.84 \pm 2.83	3.99
J22560985+6243379	22:56:09.88	62:43:38.11	-31.21 \pm 0.92	11.37
J22563371+6246468	22:56:33.73	62:46:46.69	-2.15 \pm 3.31	2.95
J22552722+6243290	22:55:27.23	62:43:28.92	-11.74 \pm 4.74	6.29
J22560030+6245029	22:56:01.27	62:44:56.88	-2.07 \pm 1.40	7.30
J22562963+6245284	22:56:29.64	62:45:28.52	-9.57 \pm 2.37	6.11
J22571517+6245499	22:57:15.19	62:45:50.06	-19.88 \pm 5.44	1.86
J22563906+6245092	22:56:39.04	62:45:09.22	20.64 \pm 2.42	4.14
J22571391+6241355	22:57:13.89	62:41:35.44	50.91 \pm 5.73	1.89

Table 5
(Continued)

2MASS ID	R.A. (J2000)	Decl. (J2000)	RV $\pm \sigma$ (km s ⁻¹)	R Value
J22564067+6242109	22:56:40.65	62:42:10.91	-66.88 \pm 0.77	13.73
J22562134+6243257	22:56:21.34	62:43:25.71	-12.90 \pm 5.30	4.50
J22565123+6243197	22:56:51.24	62:43:19.74	-11.04 \pm 3.76	4.98
J22561535+6242268	22:56:15.34	62:42:27.04	-12.38 \pm 1.17	9.29
J22571812+6237011	22:57:18.14	62:37:00.98	-25.59 \pm 1.05	9.84
J22562657+6241574	22:56:26.58	62:41:57.41	-45.03 \pm 2.07	4.98
J22562637+6241289	22:56:26.38	62:41:28.94	-13.97 \pm 1.40	8.31
J22570594+6238180	22:57:05.96	62:38:18.05	-15.67 \pm 1.92	6.00
J22563654+6240077	22:56:36.55	62:40:07.52	50.66 \pm 2.77	3.65
J22554285+6242312	22:55:42.86	62:42:30.97	-33.58 \pm 0.86	11.56
J22553311+6240593	22:55:33.10	62:40:59.21	-22.40 \pm 4.18	1.16
J22562974+6238533	22:56:29.74	62:38:53.37	-10.48 \pm 1.28	8.32
J22555016+6240070	22:55:50.18	62:40:07.26	-10.35 \pm 1.11	10.8
J22564271+6237475	22:56:42.73	62:37:47.51	-28.33 \pm 5.58	1.80
J22563167+6237526	22:56:31.70	62:37:52.54	-18.39 \pm 1.75	7.46
J22565692+6236389	22:56:56.91	62:36:38.80	-14.70 \pm 10.37	1.35
J22560969+6237289	22:56:09.69	62:37:29.05	-35.18 \pm 5.88	1.52
J22570845+6225441	22:57:08.44	62:25:44.29	-83.85 \pm 0.65	15.82
J22570709+6230189	22:57:07.08	62:30:19.05	-17.24 \pm 4.77	2.95
J22562274+6232501	22:56:22.77	62:32:50.12	-13.19 \pm 5.34	1.57
J22561318+6235331	22:56:13.19	62:35:33.16	3.34 \pm 2.50	4.10
J22555010+6237443	22:55:50.12	62:37:44.52	-5.19 \pm 4.05	6.29
J22563234+6232404	22:56:32.37	62:32:40.44	3.65 \pm 1.82	5.07
J22571116+6227330	22:57:11.15	62:27:33.00	... \pm
J22570603+6225208	22:57:06.05	62:25:20.84	-33.78 \pm 1.25	8.19
J22554655+6233432	22:55:46.59	62:33:43.24	-46.02 \pm 0.80	13.00
J22565217+6226391	22:56:52.18	62:26:39.07	3.96 \pm 4.36	1.36
J22560135+6231397	22:56:01.36	62:31:39.52	-52.00 \pm 0.74	14.16
J22552759+6241028	22:55:27.58	62:41:02.70	-40.12 \pm 0.94	10.77
J22555686+6234332	22:55:56.85	62:34:33.24	20.33 \pm 3.63	3.05
J22553701+6237109	22:55:37.12	62:37:17.38	-36.14 \pm 0.92	11.52
J22553503+6235312	22:55:35.02	62:35:31.05	-104.19 \pm 0.85	12.46
J22551738+6241070	22:55:17.40	62:41:06.94	-12.08 \pm 5.19	0.69
J22552505+6236511	22:55:25.04	62:36:51.19	-11.53 \pm 1.46	7.51
J22553247+6231367	22:55:32.43	62:31:36.71	-20.45 \pm 6.31	2.13
J22555006+6223083	22:55:50.06	62:23:08.26	-14.02 \pm 4.15	4.34
J22545509+6233404	22:54:55.13	62:33:40.13	-29.54 \pm 1.05	9.85
J22550059+6235221	22:55:00.60	62:35:22.06	-8.63 \pm 1.00	10.82
J22551657+6232522	22:55:16.59	62:32:52.13	-28.72 \pm 4.32	1.85
J22550590+6234504	22:55:05.91	62:34:50.53	-10.10 \pm 2.77	6.97
J22550975+6239074	22:55:09.71	62:39:07.24	29.33 \pm 6.39	3.09
J22543882+6223364	22:54:38.83	62:23:36.62	-11.17 \pm 0.83	12.57
J22543713+6226052	22:54:37.18	62:26:05.50	-5.87 \pm 0.97	10.22
J22540555+6223064	22:54:05.54	62:23:06.65	-28.15 \pm 0.98	10.87
J22545903+6237177	22:54:59.04	62:37:17.82	0.88 \pm 10.67	3.83
J22542760+6225270	22:54:27.60	62:25:26.88	-5.50 \pm 2.60	4.56
J22541824+6226460	22:54:18.24	62:26:45.93	5.93 \pm 8.75	2.48
J22542257+6225041	22:54:22.56	62:25:04.03	-13.77 \pm 1.77	7.82
J22531916+6225326	22:53:19.20	62:25:32.83	17.33 \pm 1.17	9.06
J22542405+6235158	22:54:24.05	62:35:15.95	-14.11 \pm 2.62	5.81
J22544431+6235183	22:54:44.32	62:35:18.23	12.42 \pm 0.92	11.68
J22565314+6232094	22:54:33.12	62:33:33.84	4.54 \pm 1.45	7.23
J22541607+6230398	22:54:16.08	62:30:39.76	-19.88 \pm 1.02	10.33
J22543423+6235555	22:54:34.20	62:35:55.46	-4.98 \pm 6.67	3.47
J22534870+6236019	22:53:48.70	62:36:01.81	-11.92 \pm 1.38	8.27
J22544294+6238557	22:54:42.93	62:38:55.74	-1.53 \pm 2.27	5.51
J22534931+6235274	22:53:49.29	62:35:27.52	-9.69 \pm 1.53	7.85
J22533629+6231446	22:53:36.28	62:31:44.69	-12.69 \pm 1.58	8.31
J22523242+6227422	22:52:32.41	62:27:42.40	-3.32 \pm 15.06	1.18
J22544332+6240103	22:54:43.31	62:40:10.26	-10.47 \pm 1.85	6.37
J22540553+6235451	22:54:05.56	62:35:45.03	-10.99 \pm 4.59	1.94
J22523057+6226259	22:52:30.58	62:26:25.86	8.59 \pm
J22530352+6237081	22:53:03.52	62:37:08.00	-16.42 \pm 8.63	0.73
J22540731+6238098	22:54:06.84	62:38:06.57	-45.49 \pm 1.32	7.63

Table 5
(Continued)

2MASS ID	R.A. (J2000)	Decl. (J2000)	RV $\pm \sigma$ (km s ⁻¹)	R Value
J22530628+6236326	22:53:06.30	62:36:32.69	-13.22 \pm 6.26	0.65
J22540271+6238389	22:54:02.70	62:38:39.06	-27.36 \pm 0.93	10.69
J22534450+6238305	22:53:44.50	62:38:30.41	-25.15 \pm 16.73	0.78
J22523176+6231194	22:52:31.80	62:31:19.69	-2.13 \pm 1.42	6.79
J22524589+6234125	22:52:45.92	62:34:12.53	57.21 \pm 3.88	1.31
J22533602+6236494	22:53:36.02	62:36:49.34	-20.27 \pm 7.09	1.46
J22524939+6233534	22:52:49.40	62:33:53.57	-30.23 \pm 1.69	5.82
J22534448+6239061	22:53:44.44	62:39:06.52	-19.65 \pm 2.62	4.09
J22524772+6240044	22:52:47.71	62:40:04.72	1.69 \pm 8.11	1.58
J22530063+6237581	22:53:00.63	62:37:58.14	30.89 \pm 2.00	5.61
J23033097+6239264	22:52:32.32	62:39:25.12	-31.47 \pm 1.76	5.22
J22531297+6238444	22:53:13.00	62:38:44.41	30.05 \pm 1.47	7.91
J22543623+6241336	22:54:36.24	62:41:33.81	-39.31 \pm 2.33	4.24
J22530993+6239119	22:53:09.92	62:39:12.17	0.17 \pm 2.68	3.41
J22523061+6238279	22:52:30.61	62:38:28.16	-19.52 \pm 3.09	2.98
J22533857+6244222	22:53:38.60	62:44:22.21	-18.58 \pm 1.82	5.49
J22525023+6240458	22:52:50.26	62:40:45.98	-49.40 \pm 1.38	7.40
J22535512+6243368	22:53:55.12	62:43:36.90	-14.02 \pm 4.03	1.27
J22522749+6241104	22:52:27.48	62:41:10.30	15.96 \pm 5.39	0.79
J22523381+6243331	22:52:32.67	62:43:37.18	-22.10 \pm 2.36	3.74
J22541786+6242328	22:54:17.85	62:42:32.91	-107.30 \pm 1.02	9.91
J22535737+6243018	22:53:57.38	62:43:01.84	-61.13 \pm 0.88	11.35
J22522631+6242084	22:52:26.33	62:42:08.72	0.48 \pm 0.78	12.95
J22531323+6242295	22:53:13.27	62:42:29.46	-36.62 \pm 4.85	1.47

inform a discussion of the dynamical status and fate of the subclusters in subsequent sections.

4.1. RV Analysis of Membership

Due to the low extinction through the cluster, Hectoschelle can detect both foreground and background objects in the field in addition to members of the cluster. We therefore break up the sample into two categories: objects with youth indicators and objects without youth indicators, most of which are likely contaminants. Youth indicators are the presence of an infrared excess, implying the presence of a dusty disk or envelope (i.e., class II objects, transition-disk objects, or protostars), or detectable X-ray emission due to an active corona. The objects with X-ray emission but no IR excess are diskless pre-main-sequence (pre-MS) stars (class III objects). The velocities of the stars with youth indicators show a clear peak in the RV of -10 km s⁻¹ bin with a narrow RV distribution (Figure 3).

Objects without youth indicators may also be class III objects; however, such objects are indistinguishable from background giants or foreground dwarf objects on the basis of photometry alone. Figure 3 shows histograms for objects with youth indicators and objects without youth indicators. The objects with youth indicators show a clear peak at -10 km s⁻¹. In contrast, the histogram of the objects without youth indicators (169) shows a broad distribution of RVs ranging from -107 to 50 km s⁻¹. There is a peak at -30 km s⁻¹, which is consistent with the RVs of stars in the Perseus arm behind Cep OB3b. At the velocity of the cluster, -10 km s⁻¹, the distribution of the objects without youth indicators is relatively flat compared to the youth indicators, consistent with objects dominated by field stars. Thus, we see no clear evidence for a large number of missed class III objects lacking X-ray detection in the RV distribution, and we do not use RV as an additional criterion for membership.

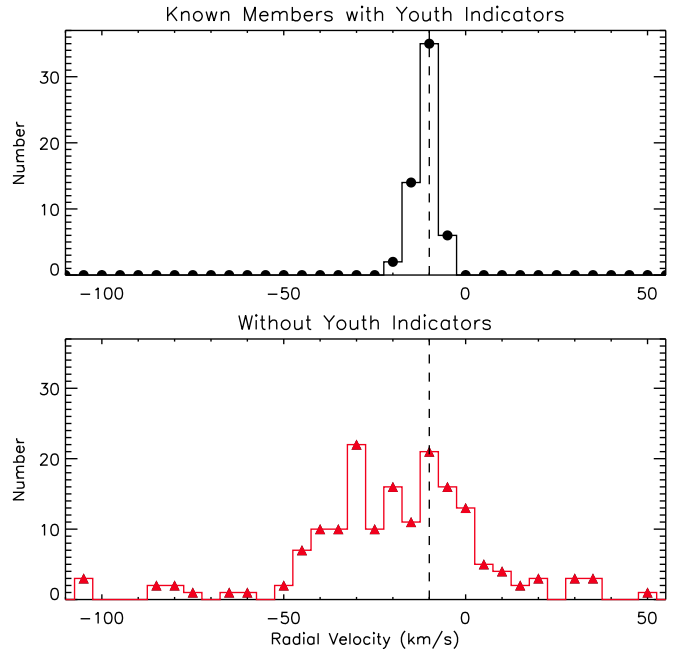


Figure 3. Radial velocity distribution of objects with youth indicators (top) and objects lacking youth indicators (bottom). The molecular cloud peaks at -10 km s⁻¹, which agrees with the LSR of the molecular cloud. More local clouds like Cep OB3b are found closer to 0 km s⁻¹. Objects with highly negative RVs are likely background stars, with objects in the Perseus arm peaking at -30 km s⁻¹.

Heyer et al. (1996) imaged ¹³CO and ¹²CO $J = 1-0$ emission from visible H II regions, which included Cep OB3b. The ¹²CO gas toward the cluster was measured at -12.7 ,

Table 6
2013 RV Results

2MASS ID	R.A. (J2000)	Decl. (J2000)	RV $\pm \sigma$ (km s ⁻¹)	R Value
J22562637+6241289	22:56:26.37	62:41:28.97	-10.59 \pm 1.63	7.30
J22560480+6239460	22:56:04.80	62:39:46.09	-9.73 \pm 1.00	9.98
J22571825+6243042	22:57:18.25	62:43:04.27	-11.13 \pm 2.17	4.56
J22562231+6240488	22:56:22.31	62:40:48.81	-9.85 \pm 1.35	7.90
J22570134+6242133	22:57:01.35	62:42:13.39	11.91 \pm 4.25	2.77
J22570594+6238180	22:57:05.95	62:38:18.07	-13.39 \pm 2.49	3.43
J22570917+6238560	22:57:09.18	62:38:56.06	-16.38 \pm 4.78	2.88
J22565186+6239521	22:56:51.86	62:39:52.12	-14.38 \pm 1.81	6.48
J22563527+6239074	22:56:35.27	62:39:07.45	-7.01 \pm 1.30	9.09
J22564210+6236207	22:56:42.10	62:36:20.73	-16.31 \pm 1.83	5.28
J22564271+6237475	22:56:42.71	62:37:47.52	-11.78 \pm 3.74	2.51
J22554154+6239030	22:55:41.54	62:39:03.07	19.25 \pm 4.88	2.05
J22564720+6237055	22:56:47.20	62:37:05.56	-5.47 \pm 2.24	7.81
J22555010+6237443	22:55:50.10	62:37:44.32	-9.30 \pm 2.45	8.34
J22561343+6236452	22:56:13.43	62:36:45.20	-17.69 \pm 3.26	3.04
J22570919+6233337	22:57:09.20	62:33:33.75	1.81 \pm 10.08	3.20
J22562852+6232301	22:56:28.52	62:32:30.11	1.46 \pm 1.19	9.03
J22561318+6235331	22:56:13.18	62:35:33.15	12.59 \pm 2.08	4.65
J22571251+6228058	22:57:12.51	62:28:05.84	-51.42 \pm 0.69	15.11
J22555686+6234332	22:55:56.86	62:34:33.29	22.35 \pm 1.49	7.88
J22561122+6233290	22:56:11.22	62:33:29.08	-30.20 \pm 7.49	1.96
J22560790+6230425	22:56:07.91	62:30:42.59	-10.36 \pm 1.97	5.29
J22554370+6234569	22:55:43.70	62:34:56.97	-14.83 \pm 0.55	19.03
J22553370+6233093	22:55:33.70	62:33:09.34	-25.55 \pm 1.44	9.28
J22553606+6238563	22:55:36.25	62:39:02.35	-6.12 \pm 5.42	4.23
J22552505+6236511	22:55:25.05	62:36:51.16	-11.19 \pm 1.45	8.41
J22550059+6235221	22:55:00.60	62:35:22.17	-9.93 \pm 1.03	9.67
J22550590+6234504	22:55:05.90	62:34:50.47	-23.59 \pm 2.57	4.90
J22545364+6234031	22:54:53.64	62:34:03.10	-18.24 \pm 2.54	6.32
J22535527+6233218	22:53:55.27	62:33:21.85	-16.36 \pm 8.71	2.36
J22544224+6235548	22:54:42.24	62:35:54.89	-8.70 \pm 1.09	9.57
J22525012+6227336	22:52:50.12	62:27:33.64	-3.87 \pm 7.60	1.13
J22552178+6237535	22:55:21.78	62:37:53.55	-5.31 \pm 6.22	1.59
J22543423+6235555	22:54:34.23	62:35:55.55	-17.14 \pm 6.54	2.57
J22531578+6235262	22:53:15.78	62:35:26.27	-22.32 \pm 6.54	1.17
J22541270+6235379	22:54:12.70	62:35:37.95	-23.91 \pm 6.71	3.44
J22532187+6234490	22:53:21.87	62:34:49.04	-22.64 \pm 2.63	3.28
J22535132+6235184	22:53:51.32	62:35:18.43	-9.67 \pm 1.21	8.42
J22523829+6232503	22:52:38.29	62:32:50.32	12.30 \pm 1.01	9.02
J22532653+6240134	22:53:26.53	62:40:13.45	-8.52 \pm 1.14	9.33
J22543166+6237117	22:54:31.66	62:37:11.69	-6.16 \pm 1.83	6.03
J22540382+6238211	22:54:03.82	62:38:21.11	-13.10 \pm 1.00	10.6
J22530421+6236112	22:53:04.22	62:36:11.26	-22.52 \pm 6.14	2.14
J22530063+6237581	22:53:00.64	62:37:58.19	-22.68 \pm 0.96	11.23
J22531015+6236444	22:53:10.15	62:36:44.42	-11.57 \pm 2.96	4.68
J22532283+6237409	22:53:22.83	62:37:40.97	-9.94 \pm 2.21	5.19
J22533869+6237171	22:53:38.69	62:37:17.11	-12.45 \pm 4.94	4.20
J22544942+6239227	22:54:49.42	62:39:22.78	-12.36 \pm 1.03	10.40
J22531480+6244040	22:53:14.80	62:44:04.05	-38.09 \pm 0.85	12.05
J22542993+6240335	22:54:29.93	62:40:33.55	-7.88 \pm 1.67	6.96
J22530099+6243548	22:53:01.00	62:43:54.82	1.69 \pm 4.33	3.60
J22555158+6239116	22:55:51.58	62:39:11.69	-6.92 \pm 1.38	7.69
J22535512+6243368	22:53:55.12	62:43:36.88	-20.39 \pm 17.09	0.23
J22551643+6240321	22:55:16.43	62:40:32.13	-8.07 \pm 0.99	10.30
J22550275+6241499	22:55:02.75	62:41:49.96	-15.14 \pm 3.54	1.42
J22550959+6244210	22:55:09.60	62:44:21.03	-21.37 \pm 4.58	5.19
J22550561+6244055	22:55:05.61	62:44:05.56	-26.24 \pm 7.41	2.67
J22544992+6251217	22:54:49.92	62:51:21.78	-10.45 \pm 1.52	9.46
J22552722+6243290	22:55:27.22	62:43:29.03	-14.88 \pm 4.14	7.02
J22551760+6243231	22:55:17.60	62:43:23.18	-10.45 \pm 2.77	6.94
J22552486+6246446	22:55:24.86	62:46:44.63	6.10 \pm 4.81	2.88
J22560150+6247467	22:56:01.50	62:47:46.79	-10.70 \pm 1.57	7.81
J22555228+6249200	22:55:52.28	62:49:20.07	-6.41 \pm 0.88	10.9
J22555152+6245053	22:55:51.52	62:45:05.40	-9.88 \pm 1.32	7.77

Table 6
(Continued)

2MASS ID	R.A. (J2000)	Decl. (J2000)	RV $\pm \sigma$ (km s ⁻¹)	R Value
J22561829+6245166	22:56:18.29	62:45:16.62	-17.19 \pm 4.97	3.01
J22560391+6243359	22:56:03.92	62:43:35.90	-11.24 \pm 1.13	8.78
J22563677+6255599	22:56:36.77	62:55:59.94	-16.43 \pm 4.40	4.63
J22554749+6241576	22:55:47.49	62:41:57.61	-13.00 \pm 2.43	5.38
J22560068+6245310	22:56:00.69	62:45:31.02	-9.43 \pm 1.37	6.70
J22562134+6243257	22:56:21.34	62:43:25.72	6.65 \pm 9.85	2.44
J22560428+6242388	22:56:04.28	62:42:38.85	-9.92 \pm 21.54	1.49
J22564512+6246193	22:56:45.12	62:46:19.32	-10.50 \pm 2.09	6.02
J22562963+6245284	22:56:29.63	62:45:28.44	-11.15 \pm 2.29	6.02
J22565123+6243197	22:56:51.23	62:43:19.76	-11.81 \pm 2.68	5.33
J22555016+6240070	22:55:50.16	62:40:07.09	-9.56 \pm 1.60	6.67
J22564619+6244225	22:56:46.19	62:44:22.59	-15.71 \pm 1.31	8.04
J22561535+6242268	22:56:15.35	62:42:26.86	-13.04 \pm 1.04	10.16

-11.4, -10.1, -8.8, and -7.5 km s⁻¹, which is consistent with the motions of the members. We do not see a significant offset between the stellar motions and the gas motions, further confirmation of their association with the cloud.

4.2. Subcluster Sizes, Structures, and Densities

To characterize the structures of the subclusters, we apply an analytic model developed by King (1962) for globular clusters. The models are parameterized by a core radius, an outer tidal radius, and a central peak density. Although this model is not appropriate for the elongated and irregular structure of more deeply embedded clusters such as the ONC (Kuhn et al. 2014; Megeath et al. 2016), the more circular symmetry of the two Cep OB3b subclusters motivates the use of this model. We use the *Chandra* and *Spitzer* data for the King model fits. We adopt the center positions of the subclusters given by the method of Gutermuth et al. (2009). The algorithm isolates the two most numerous YSO overdensities that lack further substructure using the catalog and field-of-view limits of Allen et al. (2012). We compute the azimuthally averaged radial surface density profile in 0.3 pc bins and fit them with King models using the IDL implementation of mpfit, specifically the mpcurvefit.pro module (Markwardt 2009).

Since the larger annuli extended in part past the *Chandra* field of view, we must correct for the missing *Chandra* objects. We do this by measuring the density of the X-ray objects for the section of the annulus within the *Chandra* field of view. In addition, we must correct for the stars that did not have infrared excesses and did not have bright enough X-ray emissions to be detected by *Chandra*. Allen et al. (2012) determined disk fractions in each subcluster using visible color-magnitude diagrams and the X-ray data (see Table 5 Allen et al. 2012). We adopt the upper and lower values of the disk fractions for each subcluster to correct for missing objects. We do this by determining a correction factor for each subcluster, given by the equation

$$\eta = \frac{1}{f_{\text{disk}} N_{\text{IR}} + N_{\text{X-ray}}}, \quad (1)$$

where N_{IR} is the number of IR-excess objects with the boundary of the given subclusters, $N_{\text{X-ray}}$ is the number of *Chandra* objects, and f_{disk} is the disk fraction. This assumes that $N_{\text{IR}}/f_{\text{disk}}$ gives the total number of objects. Finally, we take

the total number of stars from the *Chandra* and *Spitzer* data sets in each subcluster and subtract off a 15.5 pc⁻² baseline density. This was done to (1) exclude the larger scale halo of YSOs that are likely part of the larger Cep OB3b cluster and (2) to keep the two subclusters separate. After the 15.5 pc⁻² baseline density is subtracted, the measured densities are multiplied by the correction factor to determine the corrected density of stars in each annulus. This yields 809 and 664 stars for disk fractions of 0.32 and 0.39, respectively, in the east and 501 and 416 stars for disk fractions of 0.44 and 0.53, respectively, in the west. The number of objects determined here are used in the potential energy calculations.

The fits give different results for the two subclusters (Figure 4, Table 8). The core radii are 1.36 \pm 0.30 pc and 0.52 \pm 0.11 pc for the east and west, respectively. The tidal radii are 2.32 \pm 0.19 pc and 3.1 \pm 1.0 pc for the east and west, respectively. We note that the tidal radius usually refers to the radius at which the tidal field of the galaxy dominates over the gravity of the cluster, separating stars out of the cluster. Here, the tidal radius defines the edge of the subclusters in the King model, and we will refer to it as the subcluster radius throughout the remainder of the paper.

In the above analysis, we have assumed that the two subclusters are circularly symmetric. To test how closely the clusters follow this assumption, we compute the AAP from Gutermuth et al. (2005) for the two subclusters. The value of the AAP measures the deviation of the azimuthal distribution of stars from circular symmetry. We find values of 1.155 and 1.724 for the east and west, respectively. This shows that the surface density distribution of stars in the west deviate significantly from circular symmetry and that the subcluster is significantly elongated. In comparison, the east appears circularly symmetric with a relatively smooth distribution of stars.

The stellar peak densities are 521 and 428 stars pc⁻² in the east and 342 and 284 stars pc⁻² in the west, depending on the disk fraction. The average stellar surface densities within the core radii are 240 and 197 stars pc⁻² in the east and 220 and 182 stars pc⁻² in the west, depending on the disk fraction. From these values, the east is significantly richer in members than the west and is circularly symmetric, showing a larger core radius. The west is characterized by elongation, a core radius that is less than half of that for the east, and has fewer members.

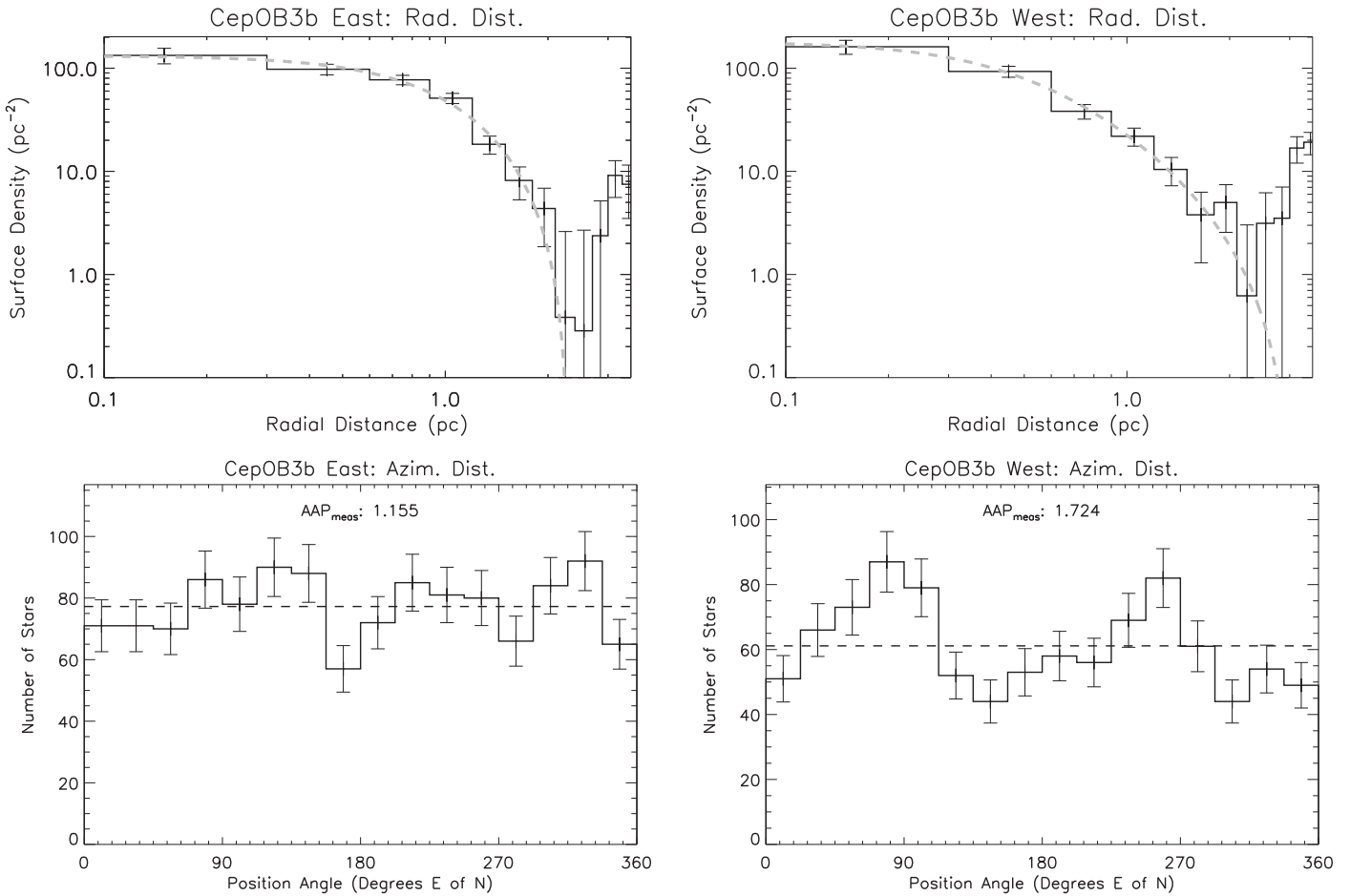


Figure 4. The best-fit 1962 King models. The top-left and -right plots are the uncorrected surface density vs. radial distance for the east and west subclusters, respectively. The bottom-left and -right plots are the number of stars vs. position angle for the east and west subclusters, respectively. The deviation of these from circular symmetry, which is given by the dashed line, determines the value of the azimuthal parameter (AAP; Gutermuth et al. 2005).

From the King model fits, the half-mass radius is 0.83 and 0.67 pc for the east and west, respectively.

4.3. The Velocity Structure of the Cep OB3b Cluster

The position–velocity (PV) diagrams of the Cep OB3b cluster are shown in Figures 5 and 6; the positions of these stars in the subclusters are given in Figure 7. These figures indicate the lack of an apparent velocity gradient in decl. or R.A. for both subclusters and the entire region itself. The RVs in the west have a relatively flat distribution around the average RV. On the other hand, the east has a much wider spread of RVs but still lacks an RV gradient in R.A. or decl.

The average RV of the two subclusters are very similar, -12.09 km s^{-1} , with a standard error of the mean as 0.56 km s^{-1} , and -10.86 km s^{-1} , with a standard error of the mean as 0.54 km s^{-1} for the east and west, respectively. These are within 2σ of each other. The overall RV average is -11.69 km s^{-1} with a standard error of the mean as 0.42 km s^{-1} .

4.4. The Velocity Dispersion of the Subclusters

To constrain the velocity dispersions of the subclusters, we implement a Bayesian parameter estimation for the velocity dispersion in each subcluster. We determine the likelihood function using a Monte Carlo comparison to our measured

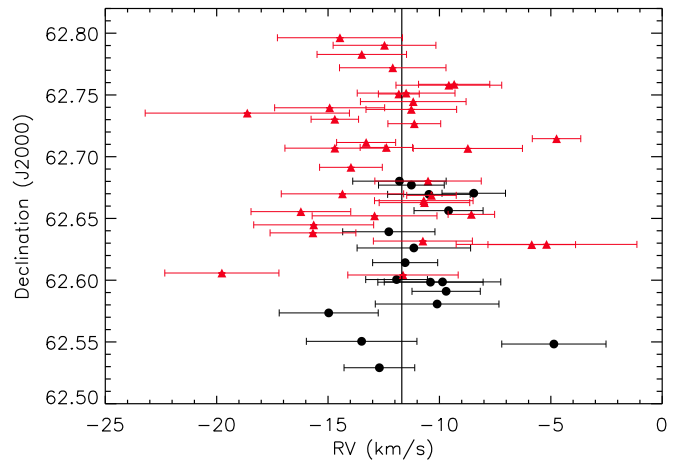


Figure 5. Decl. vs. RV for stars with youth indicators. The red triangles are objects in the east subcluster. The black circles are objects in the west subcluster.

velocity dispersions for the 35 and 17 stars of the eastern and western subclusters, respectively. The number of stars in each sub-cluster are determined by Figure 7, where member stars that are not potential binaries and have a $R \geq 5$ are shown with respect to the eastern and western subcluster radii. We start by

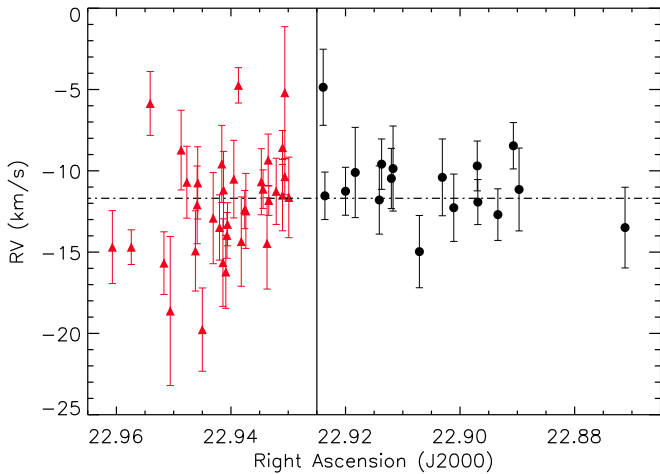


Figure 6. Radial velocity vs. R.A. for objects with youth indicators. The symbols and colors are the same as in Figure 5.

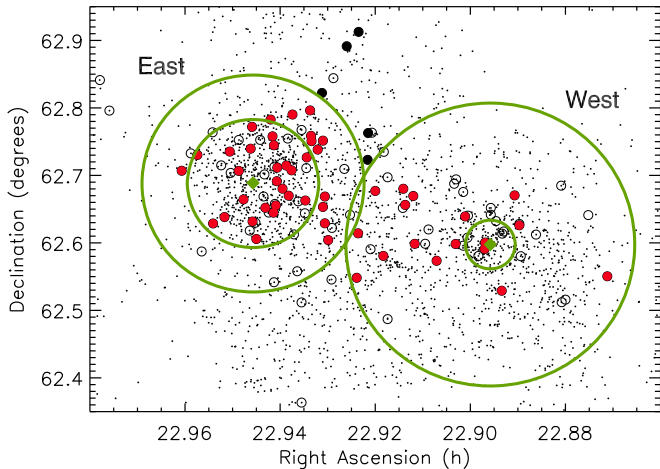


Figure 7. The black points are all the members of Cep OB3b (Allen et al. 2012), and the open circles have Hectoschelle spectra. The filled black circles are members with Hectoschelle spectra that survived the cuts described in Section 2, but fall outside the subcluster radii. The filled red circles are members with Hectoschelle spectra within the subcluster radii and are used in the kinematic analysis. The green diamonds are the centers of the respective subclusters and the green circles are the core and subcluster radii for each subcluster.

adopting 1D Gaussian velocity distributions centered on the RV of each subcluster; the distributions of the subclusters have independent velocity dispersions, σ . To calculate the velocity dispersion, 35 RVs and 17 RVs are randomly drawn from the Gaussian distribution of the east and west, respectively. We iterate this process, changing the width σ of the Gaussian distribution. For each subcluster, the σ starts at 0.05 km s^{-1} and increases in steps of 0.05 km s^{-1} until $\sigma = 10 \text{ km s}^{-1}$ is reached. The RVs were drawn 10,000 times for each value of σ .

To account for unresolved binaries, we adopt the approach of Cottaar et al. (2012) to add the effect of orbital motions. These would be cases without a double-lined spectrum where the velocities that we measure are those of the more luminous primary stars. We adopt three mass-based ($1 M_{\odot}$, $0.75 M_{\odot}$, $0.5 M_{\odot}$) log-normal velocity distributions. The solar-type distribution of absolute velocities has a log-normal width of $0.84 \log_{10} \text{ km s}^{-1}$ and a mean of $0.08 \log_{10} \text{ km s}^{-1}$ (Cottaar et al. 2012).

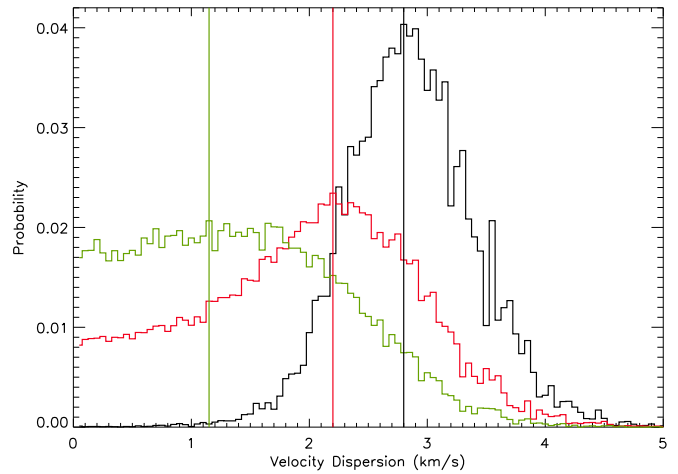


Figure 8. The PDF of the velocity distribution in the east subcluster. The black histogram is the PDF for a binary fraction of 0 with a peak velocity dispersion value of 2.8 km s^{-1} , the red for a binary fraction of 0.5 with a peak velocity dispersion value of 2.2 km s^{-1} , and the green for a binary fraction of 1.0 with a peak velocity dispersion value of 1.15 km s^{-1} . The vertical lines represent the peak value of the distribution. Changing the binary fraction has a significant effect on the PDF of the velocity dispersion.

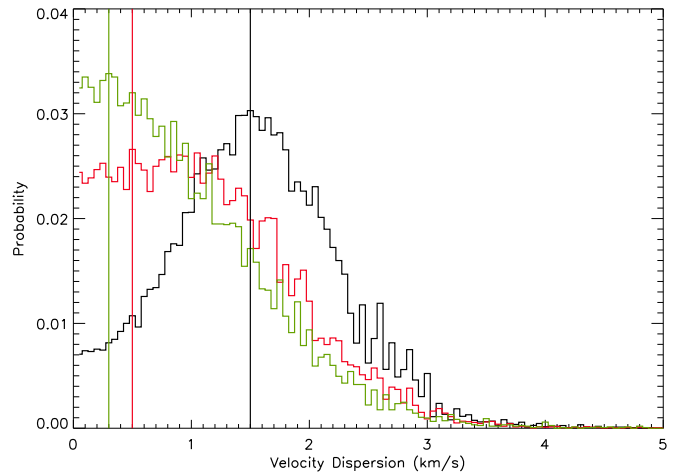


Figure 9. The PDF of the velocity distribution in the west subcluster. The black histogram is the PDF for a binary fraction of 0 with a peak velocity dispersion value of 1.5 km s^{-1} , the red for a binary fraction of 0.5 with a peak velocity dispersion value of 0.5 km s^{-1} , and the green for a binary fraction of 1.0 with a peak velocity dispersion value of 0.3 km s^{-1} . The vertical lines represent the peak value of the distribution. Changing the binary fraction has little effect on the resulting velocity dispersion.

The $0.75 M_{\odot}$ ($0.62 \log_{10} \text{ km s}^{-1}$ width and $0.35 \log_{10} \text{ km s}^{-1}$ mean) and $0.5 M_{\odot}$ ($0.15 \log_{10} \text{ km s}^{-1}$ width and $0.52 \log_{10} \text{ km s}^{-1}$ mean) distributions are scaled from the solar-type distribution by implementing Equation (3) in Cottaar et al. (2012) and using the orbital period distributions from Table 1 in Duchêne & Kraus (2013). Using the spectral types from T. S. Allen et al. (2018, in preparation), we estimate the masses of the 35 (17) members and assign them to the appropriate mass-based binary velocity distribution. A total of 13 objects fall into the solar-type bin, 15 fall into the $0.75 M_{\odot}$ bin, and 24 fall into the $0.5 M_{\odot}$ bin.

We test three binary fractions: 0, 0.5, and 1. Stars are randomly assigned a binary motion from the appropriate mass-based Gaussian distribution. The typical FWHM of the cross-correlation plots is $\sim 40 \text{ km s}^{-1}$. We throw out binary motions

Table 7
Potential Spectroscopic Binary Candidates

2MASS ID	R.A. (J2000)	Decl. (J2000)	RV $\pm \sigma$ (km s ⁻¹)
J22553151+6253093	22:55:32.52	62:53:09.48	-22.13 \pm 4.20
J22550645+6241517	22:55:06.47	62:41:51.78	15.38 \pm 2.25
J22560723+6245358	22:56:07.23	62:45:35.76	-15.69 \pm 6.15
J22552722+6243290	22:55:27.23	62:43:28.90	15.19 \pm 5.35
J22561571+6242509	22:56:15.72	62:42:51.08	-12.90 \pm 2.57
J22560574+6242599	22:56:05.75	62:42:59.74	6.90 \pm 2.83
J22570068+6245485	22:57:00.70	62:45:48.44	-20.45 \pm 10.68
J22563906+6245092	22:56:39.04	62:45:09.22	36.56 \pm 1.55
J22564077+6245453	22:56:40.74	62:45:45.36	-46.79 \pm 6.55
J22561377+6240505	22:56:13.76	62:40:50.60	-1.17 \pm 6.70
J22554154+6239030	22:55:41.54	62:39:03.11	-21.34 \pm 2.41
J22570919+6233337	22:57:09.25	62:33:33.59	7.32 \pm 8.98
J22562445+6233559	22:56:24.47	62:33:55.89	-32.36 \pm 4.09
J22555063+6228416	22:55:50.61	62:28:41.52	-18.72 \pm 5.83
J22545686+6234128	22:54:56.86	62:34:12.58	-9.17 \pm 4.53
J22545903+6237177	22:54:59.03	62:37:17.82	-18.48 \pm 3.74
J22545364+6234031	22:54:53.61	62:34:03.10	-18.92 \pm 3.56
J22535527+6233218	22:53:55.26	62:33:21.76	-21.93 \pm 6.62
J22542405+6235158	22:54:24.04	62:35:15.95	-1.88 \pm 4.77
J22523087+6231116	22:52:30.84	62:31:11.45	-13.52 \pm 6.06
J22534360+6235322	22:53:43.60	62:35:32.20	-38.99 \pm 6.97
J22540438+6235548	22:54:04.37	62:35:54.68	-11.81 \pm 5.33
J22532966+6234051	22:53:29.64	62:34:05.00	-21.55 \pm 2.01
J22535723+6236506	22:53:57.24	62:36:50.70	-58.37 \pm 2.01
J22531785+6234592	22:53:17.86	62:34:59.10	-21.64 \pm 6.49
J22533413+6238199	22:53:33.19	62:38:20.55	-28.19 \pm 4.50
J22540632+6243500	22:54:06.33	62:43:50.09	30.02 \pm 1.32
J22541162+6242285	22:54:11.63	62:42:28.55	-28.24 \pm 10.85
J22550261+6251081	22:55:01.39	62:51:11.83	-27.97 \pm 3.78
J22542910+6254472	22:54:29.07	62:54:47.07	-24.82 \pm 5.41
J22545316+6250085	22:54:53.16	62:50:08.35	-25.52 \pm 4.63
J22542993+6240335	22:54:29.92	62:40:33.57	-8.10 \pm 7.02
J22543513+6245431	22:54:35.14	62:45:43.20	-39.69 \pm 7.01
J22550915+6253570	22:55:09.14	62:53:57.12	-31.49 \pm 7.90
J22552486+6246446	22:55:24.87	62:46:44.63	33.22 \pm 3.33
J22554749+6241576	22:55:47.49	62:41:57.68	-11.94 \pm 4.73
J22564371+6242017	22:56:43.72	62:42:01.68	-12.56 \pm 5.07
J22563865+6237140	22:56:38.68	62:37:14.29	-31.93 \pm 4.52
J22555006+6223083	22:55:50.15	62:23:08.25	-16.35 \pm 4.04
J22551657+6232522	22:55:16.59	62:32:52.12	-14.09 \pm 3.57
J22522558+6222059	22:52:25.60	62:22:05.91	-14.94 \pm 6.56
J22543423+6235555	22:54:34.20	62:35:55.46	2.70 \pm 5.57
J22531578+6235262	22:53:15.78	62:35:26.13	-12.71 \pm 15.25
J22533664+6236489	22:53:36.65	62:36:48.99	-13.82 \pm 7.32
J22533869+6237171	22:53:38.67	62:37:17.23	11.21 \pm 7.64
J22550760+6244452	22:55:08.12	62:44:57.93	35.31 \pm 2.45
J22553847+6255182	22:55:37.59	62:55:19.18	49.39 \pm 7.66
J22555591+6252385	22:55:55.86	62:52:38.46	-15.80 \pm 7.92
J22562031+6254458	22:56:20.39	62:54:46.05	-17.91 \pm 1.62
J22550959+6244210	22:55:09.61	62:44:21.04	-7.00 \pm 4.12
J22561978+6248022	22:56:19.81	62:48:02.17	-2.35 \pm 3.75
J22563678+6246031	22:56:36.82	62:46:02.94	-8.02 \pm 7.08
J22562134+6243257	22:56:21.33	62:43:25.71	-12.87 \pm 3.89
J22565035+6242485	22:56:50.36	62:42:48.58	-15.15 \pm 4.60
J22570134+6242133	22:57:01.36	62:42:13.43	-12.87 \pm 13.56
J22563127+6240588	22:56:31.26	62:40:58.71	-11.92 \pm 4.30
J22542460+6225053	22:54:24.63	62:25:05.22	-25.93 \pm 1.95
J22535945+6235102	22:53:59.42	62:35:10.21	53.78 \pm 3.16
J22535969+6236320	22:53:59.69	62:36:32.03	-22.27 \pm 4.59
J22531574+6234357	22:53:15.71	62:34:35.77	-41.03 \pm 3.84
J22504792+6233227	22:50:47.94	62:33:22.62	-33.24 \pm 2.58
J22542135+6248095	22:54:21.35	62:48:09.36	-9.31 \pm 1.12
J22550804+6244252	22:55:08.05	62:44:25.41	-5.57 \pm 1.83
J22554785+6252037	22:55:47.84	62:52:03.65	-13.88 \pm 7.14

Table 7
(Continued)

2MASS ID	R.A. (J2000)	Decl. (J2000)	RV $\pm \sigma$ (km s ⁻¹)
J22561978+6248022	22:56:19.81	62:48:02.17	-13.84 \pm 2.83
J22552722+6243290	22:55:27.23	62:43:28.90	-11.74 \pm 4.74
J22563906+6245092	22:56:39.04	62:45:09.22	20.64 \pm 2.42
J22562134+6243257	22:56:21.34	62:43:25.71	-12.90 \pm 5.30
J22565123+6243197	22:56:51.24	62:43:19.74	-11.04 \pm 3.76
J22565692+6236389	22:56:56.91	62:36:38.80	-14.70 \pm 10.37
J22565217+6226391	22:56:52.18	62:26:39.07	3.96 \pm 4.36
J22555686+6234332	22:55:56.85	62:34:33.24	20.33 \pm 3.63
J22555006+6223083	22:55:50.06	62:23:08.26	-14.02 \pm 4.15
J22550975+6239074	22:55:09.71	62:39:07.24	29.33 \pm 6.39
J22545903+6237177	22:54:59.04	62:37:17.82	0.88 \pm 10.67
J22542760+6225270	22:54:27.60	62:25:26.88	-5.50 \pm 8.75
J22541824+6226460	22:54:18.24	62:26:45.93	5.93 \pm 8.75
J22542405+6235158	22:54:24.05	62:35:15.95	-14.11 \pm 2.62
J22523242+6227422	22:52:32.41	62:27:42.40	-3.32 \pm 15.06
J22530063+6237581	22:53:00.63	62:37:58.14	30.89 \pm 2.00
J22531297+6238444	22:53:13.00	62:38:44.41	30.05 \pm 1.47
J22543623+6241336	22:54:36.24	62:41:33.81	-39.31 \pm 2.33
J22570134+6242133	22:57:01.35	62:42:13.39	11.91 \pm 4.25
J22555010+6237443	22:55:50.10	62:37:44.32	-9.30 \pm 2.45
J22570919+6233337	22:57:09.20	62:33:33.75	1.81 \pm 10.08
J22561318+6235331	22:56:13.18	62:35:33.15	12.59 \pm 2.08
J22553370+6233093	22:55:33.70	62:33:09.34	-25.55 \pm 1.44
J22553606+6238563	22:55:36.25	62:39:02.35	-6.12 \pm 5.42
J22545364+6234031	22:54:53.64	62:34:03.10	-18.24 \pm 2.54
J22535527+6233218	22:53:55.27	62:33:21.85	-16.36 \pm 8.71
J22541270+6235379	22:54:12.70	62:35:37.95	-23.91 \pm 6.71
J22530063+6237581	22:53:00.64	62:37:58.19	-22.68 \pm 0.96
J22533869+6237171	22:53:38.69	62:37:17.11	-12.45 \pm 4.94
J22530099+6243548	22:53:01.00	62:43:54.82	1.69 \pm 4.33
J22550959+6244210	22:55:09.60	62:44:21.03	-21.37 \pm 4.58
J22550561+6244055	22:55:05.61	62:44:05.56	-26.24 \pm 7.41
J22552722+6243290	22:55:27.22	62:43:29.03	-14.88 \pm 4.14
J22563677+6255599	22:56:36.77	62:55:59.94	-16.43 \pm 4.40
J22562134+6243257	22:56:21.34	62:43:25.72	6.65 \pm 9.85

Table 8
King (1962) Fit Results

Subcluster	Disk Fraction	A (pc ⁻²) ¹	R_{core} (pc)	R_{tidal} (pc)	AAP _{meas}	Number of Members	Σ_{mean} stars (pc ⁻²)	Σ_{peak} (stars pc ⁻²)
East	0.32	541 \pm 202	1.36 \pm 0.30	2.32 \pm 0.19	1.155	809	240	521
East	0.39	541 \pm 202	1.36 \pm 0.30	2.32 \pm 0.19	1.155	664	197	428
West	0.44	258 \pm 42	0.52 \pm 0.11	3.1 \pm 1.0	1.724	501	220	342
West	0.53	258 \pm 42	0.52 \pm 0.11	3.1 \pm 1.0	1.724	416	182	284

Note.¹ This value has not been scaled to correct for the disk fraction.

that were greater than this because we are able to detect them in the initial RV extraction. Finally, to take into account the uncertainties in the RV measurements, we add velocities drawn from randomly sampling Gaussian distributions with σ equal to the uncertainties of the measured velocities.

We use the fraction of times the 10,000 simulated velocity distributions are within 0.1 km s⁻¹ of the actual velocity distribution to create the posterior probability density function (PDF) of the velocity dispersions. The PDFs of the velocity dispersions for the east and west are shown in Figures 8 and 9, respectively. The expectation values for the two subclusters for a binary fraction of 0.5 with $\pm 1\sigma$ confidence limits are

1.91 \pm 1.0 km s⁻¹ for the east and 1.1 $^{+0.8}_{-0.5}$ km s⁻¹ for the west. The peak values for these distributions are 2.2 \pm 1.0 km s⁻¹ and 0.5 $^{+0.8}_{-0.5}$ km s⁻¹ for the east and west, respectively.

We explore the influence of the binary fractions on the velocity dispersion of the eastern subcluster in Figure 8. The binary fraction changes the resulting velocity dispersion for the east. The velocity dispersion is centered at 2.8 km s⁻¹ for a binary fraction of zero. As the binary fraction increases the distribution widens and flattens moving closer to 0 km s⁻¹. This demonstrates that accounting for unresolved binaries is an important step to probing an accurate kinematical survey of young clusters. The western subcluster probability distribution

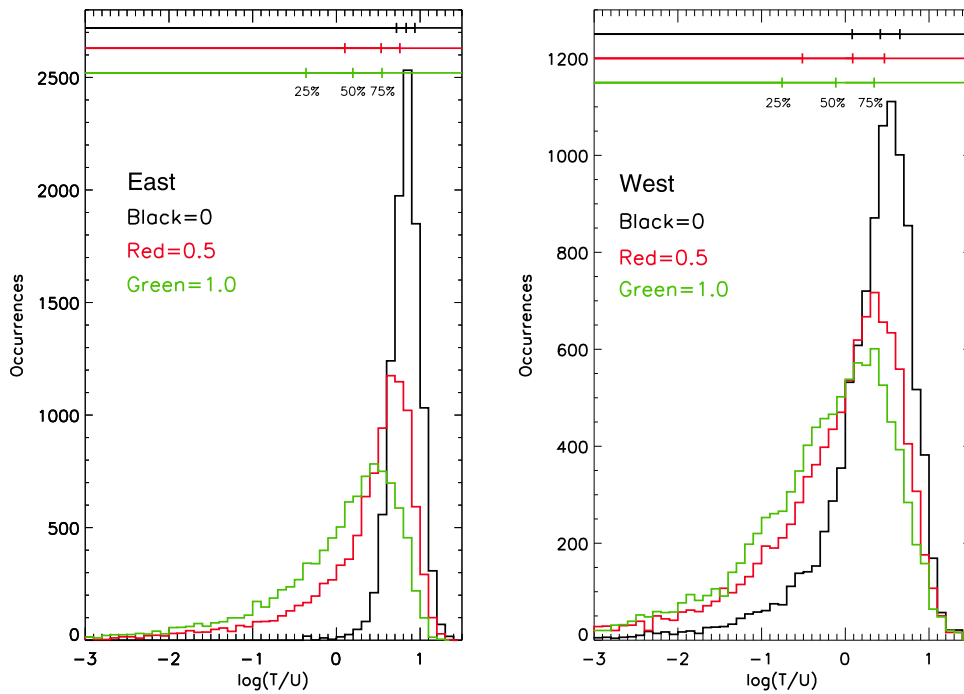


Figure 10. Plot of $\log(T/U)$ for the east (left) and west (right) subclusters from the posterior probability distribution accounting for a changing binary fraction. The black histogram for a binary fraction of 0, the red for a binary fraction of 0.5, and the green for a binary fraction of 1.0. The horizontal lines the top are marked for quartile positions in the distributions. In both cases, the peak $\log(T/U)$ evolves to a flatter and more bound distribution as the binary fraction increases.

(Figure 9) peaks at 1.5 km s^{-1} for zero binaries and moves closer to zero for binary fractions of 0.5 and 1.0, flattening and widening as in the east (Figure 8).

Jeffries et al. (2014) uses a maximum likelihood technique to account for unresolved binaries in Gamma Vel, which is adopted from Cottaar et al. (2012). Applying this approach to the Cep OB3b data, with the binary fraction set to 0.5 and the masses at $0.5 M_{\odot}$, results in an intrinsic Gaussian dispersion of $1.62 \pm 0.75 \text{ km s}^{-1}$ and $0.78 \pm 0.60 \text{ km s}^{-1}$ for the east and west, respectively. If the binary fraction is set to 0, then the dispersions increase to $2.54 \pm 0.44 \text{ km s}^{-1}$ and $0.8 \pm 0.61 \text{ km s}^{-1}$ for the east and west, respectively. The results of the velocity dispersions for the different binary fractions agree at the 1σ level between our Bayesian analysis and the maximum likelihood technique.

4.5. The Total Energy of the Eastern and Western Subclusters

We use Equation (27) in King (1962) and combine the parameter fits of the core radius, subcluster radius, and the number of stars from Section 4.2 to determine the potential energies of the subclusters. The number of stars and the subcluster radius are kept constant and only the core radius was allowed to vary because it has the largest impact on the potential energy. The value of A , the surface density of stars at the center of the cluster, is adjusted to keep the number of stars fixed to the total number of stars estimated in Section 4.2; the uncertainty in this number is taken into account by repeating the calculation with the two different disk fractions. We ran the calculation 10,000 times to create a PDF for the potential energies of each subcluster.

We adopt the PDFs of the subcluster velocity dispersions to derive kinetic energies of the subclusters 10,000 times. The kinetic energy PDFs assume a symmetric three-dimensional

velocity dispersion with the σ for the two directions in the plane of the sky equal to that in the radial direction. Thus, the total kinetic energy is given by $3/2 M_{\text{stars}} \sigma^2$. Note that the mass of stars ($0.5 M_{\odot} \times N_{\text{members}}$) appears linearly in the denominator of T/U because the mass in the kinetic energy cancels a mass in the potential energy.

For each of the 10,000 iterations, we combine the kinetic and potential energy PDFs for each subcluster to determine a final PDF of 10,000 points, i.e., $\log(T/U)$. We plot the quartiles of this distribution in Figure 10. The change in the resulting value of $\log(T/U)$ between the two disk fractions for both subclusters is insignificant, and therefore we show one disk fraction for each subcluster in Figures 10 and 11. Adopting a binary fraction of 0.5, the east $\log(T/U)$ has a mean value at 0.3 and a value at the peak of the distribution of 0.6 (Figure 11). This implies that the eastern subcluster is unbound and in a state of expansion. A binary fraction of 0 results in $\log(T/U) > 0$, also implying an unbound, expanding state. We note that unbound simply means that $\log(T/U) > 0$; it is possible that parts of the subcluster may be bound as we will discuss later. A binary fraction of 1 has a mean value in a subvirial, bound state with a probability of 61% of being unbound.

For the west subcluster, adopting a binary fraction of 0.5, results in a mean of $\log(T/U) \sim -0.16$ with a large range of outcomes and a peak value at 0.3 (Figure 11). The mean value falls into an approximate virial state with a 55% chance of an unbound state. A binary fraction of 0 results in a subvirial state with a 79% probability of being unbound. For a binary fraction of 1, the west is subvirial with roughly equal chances of being bound or unbound. From these results, the west appears to have a velocity dispersion very close to zero, depending on the binary fraction.

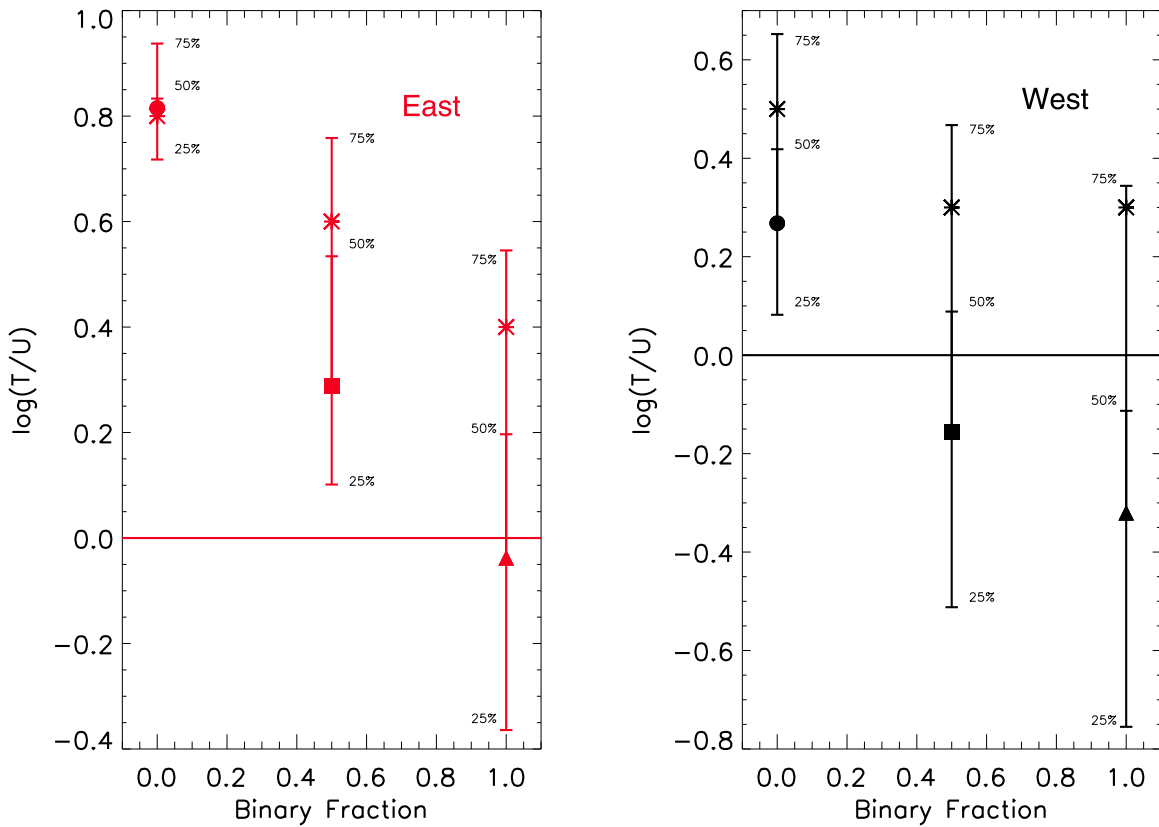


Figure 11. Plot of $\log(T/U)$ for both subclusters. The eastern subcluster is represented in red (left), and the west subcluster is represented in black (right) as a function of the adopted binary fraction. The horizontal line indicates $\log(T/U) = 0.0$; this is the dividing line between a bound and unbound cluster. The circles, squares, and triangles are the mean value for each distribution in Figure 10, and the overlaid asterisks are the values at the peaks of the distributions in Figure 10. The quartile positions that correspond to those in Figure 10 are indicated.

It is important to recall that not all of the gas mass has been expelled from Cep OB3b even though it is currently in the gas dispersal phase. Gas remains in both subclusters (see Allen et al. 2012, Figure 4). We calculate the amount of gas mass in the subclusters based on the 2MASS extinction map. Allen et al. (2014) calculated that there was roughly $1 A_v$ of foreground extinction along the line of sight to Cep OB3b. We integrate the amount of extinction greater than 2 mag inside each subcluster radius and adopt a distance of 819 pc from *Gaia* DR2 as explained below in Section 4.6. This results in $\sim 136 M_\odot$ and $\sim 697 M_\odot$ of gas mass in the east and west, respectively. The gas measured in the east is concentrated near the edge of the subcluster and is not centrally located. In contrast, the gas mass in the west is concentrated inside the core radius. The west’s mass is dominated by the gas, up to 77%, and because it is centrally concentrated, it is necessary to include the gas mass in the potential energy. Accounting for the gas mass, the $\log(T/U)$ values drop by ~ 0.4 , resulting in a subvirial, bound state, which we adopt as the more accurate kinematical result.

4.6. The Distance to Cep OB3b and the Proper Motions of the Subclusters

We cross-matched the *Gaia* DR2 catalog (Marrese et al. 2018) with Cep OB3b members with youth indicators (Allen et al. 2012) using their 2MASS IDs. We calculate the average proper motion vector components in R.A. ($\mu_{\alpha*}$) and decl. (μ_δ), where $\mu_{\alpha*}$ is $\mu_\alpha \times \cos(\delta)$. We use an R.A. of 22:54:48 to split

Table 9
GAIA DR2 Proper Motions

Subcluster	μ_α (mas yr $^{-1}$)	μ_δ (mas yr $^{-1}$)	μ_{total} (mas yr $^{-1}$)
East	-0.59 ± 0.02	-2.32 ± 0.02	2.34 ± 0.02
West	-1.25 ± 0.03	-2.78 ± 0.02	2.86 ± 0.03
Cep OB3b	-0.69 ± 0.02	-2.44 ± 0.02	2.46 ± 0.02

the stars into the two subclusters. We perform a weighted fit of a Gaussian to the distributions of proper motions. We included proper motions between -10 and 10 mas yr $^{-1}$ in bins of 0.2 mas yr $^{-1}$. The weight in each bin is given by the number of stars. The uncertainty in the mean proper motion is given by the Gaussian width normalized by the square root of the number of stars in each subcluster (696 and 370 for the east and west, respectively). The east has proper motion components of ($\mu_{\alpha*}, \mu_\delta$) equal to $(-0.59 \pm 0.02, 2.32 \pm 0.02)$ mas yr $^{-1}$, while the west subcluster has proper motion components of $(-1.25 \pm 0.02, -2.78 \pm 0.02)$ mas yr $^{-1}$ (Figure 12). The total cluster has proper motion components of $(0.69 \pm 0.02, -2.44 \pm 0.02)$ mas yr $^{-1}$. These values agree at the 1σ level with Kuhn et al. (2018). Figure 13 shows the direction of the proper motions of each subcluster with the average proper motion of the total cluster removed (also see Table 9).

To determine a distance to Cep OB3b, we used the cluster members with less than 20% uncertainty in their parallax measurements and nearby companions in the 2MASS point

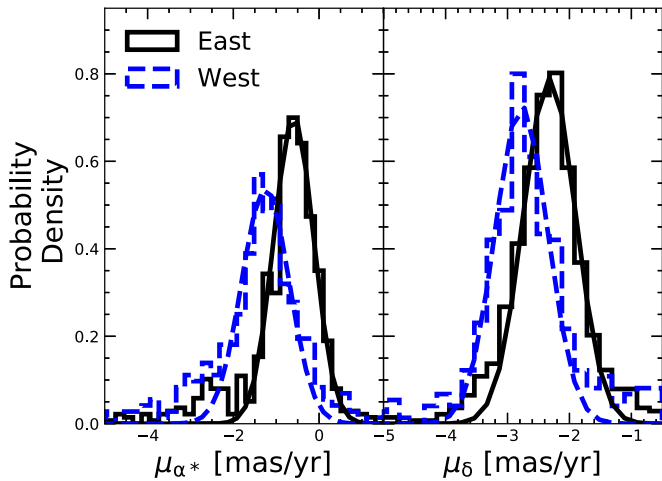


Figure 12. Histograms of the member proper motions in R.A. (left) and decl. (right) for the east (solid black) and west (dashed blue) subclusters. The bin sizes are 0.4 mas yr^{-1} . The peaks of the probability densities show that the two subclusters have different values of proper motion components: $\mu_{\alpha} = -0.59 \pm 0.02 \text{ (mas yr}^{-1}\text{)}$ and $\mu_{\delta} = -2.32 \pm 0.02 \text{ (mas yr}^{-1}\text{)}$ for the east and $\mu_{\alpha} = -1.25 \pm 0.03 \text{ (mas yr}^{-1}\text{)}$ and $\mu_{\delta} = -2.78 \pm 0.02 \text{ (mas yr}^{-1}\text{)}$ for the west. The Gaussian fits to the distributions are shown.

source catalog; the resulting histogram of parallaxes shows a clear peak (Figure 14). The parallax value correction of $0.029 \text{ mas yr}^{-1}$ was used (Lindegren et al. 2018); a distance of $819 \pm 16 \text{ pc}$ is found after correcting for the zero-point offset of the *Gaia* parallaxes. The recommended DR2 filtering to remove objects with a high excess of astrometric noise was also applied to our sample. Previous measurements have been made for the distance to Cep OB3b: $580 \pm 60 \text{ pc}$ using an age and distance ladder (Littlefair et al. 2010), 700 pc from a maser parallax-determined distance for Cepheus A (Moscadelli et al. 2009), 725 pc from near-IR color–magnitude diagrams (Sargent 1977; Getman et al. 2009), and 850 pc based on V versus $V - I$ color–magnitude diagrams (Mayne et al. 2007). The *Gaia* distance resolves the inconsistency in the distance estimates and places the cluster at the upper end of the range of previous estimates.

5. Discussion

After fitting the sizes and densities with the empirical King 1962 model and constraining the kinematics of the two subclusters, we discuss their possible early conditions, evolutionary paths up to their current state, and their potential future fates.

5.1. The Possible Early Conditions and Evolutionary Paths of the Eastern Subcluster

There is clear evidence that the east subcluster has undergone gas expulsion due to the radiation and winds of the O7 star HD 217086. The 2MASS extinction maps show that the gas measured in the east is concentrated around the edge of the subcluster and mostly dispersed in the center of the cluster (Gutermuth et al. 2011a; Allen et al. 2012). With a current number of members and gas mass as observed today, the current SFE is $\sim 73\%$; the stellar mass dominates the gravitational potential of this subcluster.

There are several reasons the east is in a state of expansion due to the gas dispersal. First, simulations of clusters after gas

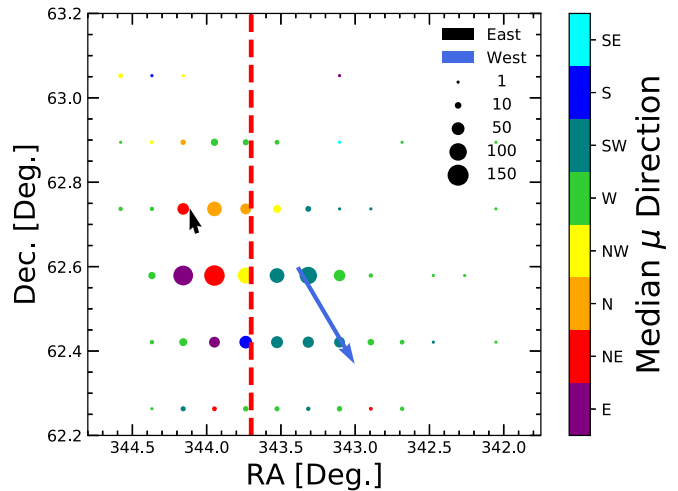


Figure 13. The total proper motions of the east (black arrow) and west (blue arrow) subclusters with the average proper motion of the total cluster removed, demonstrating that the subclusters will not merge but remain separate. The red, vertical dashed line indicates the separation in R.A. of the two subclusters. The colored dots correspond to the median parallax direction at different points in Cep OB3b with the size increasing as the number of stars in the bin agree with the direction of motion. The eastern subcluster has a total proper motion of $2.34 \pm 0.02 \text{ mas yr}^{-1}$. The western subcluster has a total proper motion of $2.86 \pm 0.03 \text{ mas yr}^{-1}$. The differential velocity exceeds the escape velocity from the more massive east.

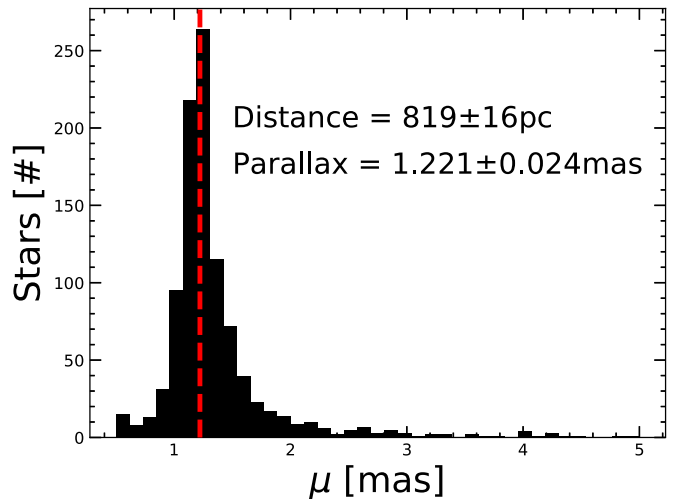


Figure 14. A histogram of objects toward Cep OB3b with parallaxes measured by *Gaia* in DR2. The median parallax is marked by the dashed, vertical red line, yielding a distance of $819 \pm 16 \text{ pc}$. We adopt this distance for Cep OB3b.

dispersal show that clusters expand significantly, with the ratio of the final to initial radii equal to the ratio of the initial to final stellar mass in the case where the cluster remains bound (Baumgardt & Kroupa 2007; Moeckel & Bate 2010). An expansion factor of five with an SFE ~ 0.2 can lead to a bound cluster if the gas dispersal timescale is slow enough, i.e., several crossing times of the cluster. Second, the circular symmetry of the cluster is unlikely due to relaxation. The crossing time at the current radius is

$$t_{\text{cross}} = R_{\text{core}} / \sigma_{1D}, \quad (2)$$

$0.74 \pm 0.16 \text{ Myr}$. This implies ~ 4 crossings have occurred since the formation of the cluster assuming an age of 3–4 Myr.

To determine the relaxation time, we use the two adopted disk fractions and

$$t_{\text{relax}} = Nt_{\text{cross}}/6\ln(N/2), \quad (3)$$

where N is the number of stars within the eastern subcluster radius. The relaxation time of the east subcluster is 16.6 ± 3.6 Myr and 14.1 ± 3.1 Myr using 809 and 664 as N , respectively. This indicates that at its current size, the east subcluster does not have time to dynamically relax, and its circular symmetry may instead come from the expansion of the cluster from a more compact, potentially more irregular, structure.

A comparison of the size and density of the eastern subcluster to those of younger clusters shows further evidence for expansion. The east has a core radius of 1.36 ± 0.30 pc, and a peak stellar surface density of 521 and 428 stars pc^{-2} . In comparison, clusters at an early stage in their gas dispersal phase have much smaller sizes and higher densities. We used a combination of *Spitzer* and *Chandra* surveys (Megeath et al. 2016) to perform the same King model fits to the ONC and the NGC 2024 cluster in the Orion B cloud, both of which still have significant amounts of molecular gas and contain massive stars. The ONC has a core radius of 0.04462 ± 0.00003 pc and a central peak stellar density of 1.12×10^6 stars pc^{-2} . NGC 2024 has a core radius of 0.0305 ± 0.0038 pc and a central peak stellar density of 5.47×10^4 stars pc^{-2} . These two clusters bracket the number of member stars contained in the east of Cep OB3b: NGC 2024 has ~ 400 dusty YSOs and the ONC has 3000 dusty YSOs, although the lower stellar density regions of this cluster extend along a 10 pc filament (Megeath et al. 2016).

More recently, Kuhn et al. (2018) found direct evidence in the proper motions from *Gaia* DR2 that the eastern subcluster, which is referred to as Cepheus B in their paper, is undergoing expansion. They measure parallaxes from 481 members and find a positive radial gradient and significant ($>3\sigma$) expansion of Cep B.

Estimating the initial size of the cluster before expansion requires several assumptions. If we assume it began in virial equilibrium ($2T = U$), it had r^{-2} density distribution and that the gas and stars have the same spatial distribution, then the outer radius of the cluster is given by $R = GM/3\sigma_{\text{TD}}^2$ (MacLaren et al. 1988), where M is the total mass. The stellar mass, determined by using $0.5 M_{\odot}$ as the average mass, for the 809 and 664 members of the east are $405 M_{\odot}$ and $332 M_{\odot}$, respectively. We adopt a total SFE of 0.2 at the onset of gas dispersal. At that point, 20% of the mass is in stars and 80% is in gas. Using $\text{SFE} = M_{\text{stars}}/M_{\text{stars}} + M_{\text{gas}}$ and solving for M_{gas} results in $1620 M_{\odot}$ and $1328 M_{\odot}$, respectively. The total masses are $2025 M_{\odot}$ and $1660 M_{\odot}$, respectively. Assuming a constant velocity dispersion of 2.2 km s^{-1} , which is the expectation value for the eastern subcluster for a binary fraction of 0.5, we obtain an initial outer radius of 0.58 pc and 0.49 pc, respectively. The subcluster radius is 2.32 pc. If we use 2.2 km s^{-1} as the velocity, then the eastern subcluster has been expanding for 0.76 Myr or 0.80 Myr, respectively. Note that the assumptions made are very simplistic. In particular, we would expect the velocity dispersion to decrease with time (Moeckel & Bate 2010). In this case, the eastern subcluster would have formed in a more compact, dense configuration with a smaller initial radius, which is consistent with

observations of younger clusters and from simulations. Furthermore, the initial SFE may range from 0.1 to 0.3 as observed in young, embedded clusters, (Megeath et al. 2016), and the initial conditions may not be virial (e.g., Farias et al. 2018). Note that the value of the SFE can depend on the spatial scale on which it is measured. The inner regions of a protocluster will have a higher SFE value than the edges (see Figure 13 in Parmentier & Pfalzner 2013).

Although most of the gas has been dispersed, star formation is continuing at the edge of the cluster. Getman et al. (2009) proposed that the O7 star is creating a radiative-driven implosion (RDI) in the rim of the associated molecular clump, resulting in continued star formation along the edge of the east; see Figure 4 in Allen et al. (2012). Although such an implosion can produce a velocity shift, our results do not detect RV gradient with respect to the location the O star; however, the gradient could be perpendicular to our line of sight and undetectable from RV motions. Given the small number of protostars in this RDI (Allen et al. 2012), this implosion may only contribute a small fraction of the cluster stars.

It seems clear that the east has expanded since formation; however, it is unclear how many of the stars form a bound cluster. Simulations and theoretical analyses show that clusters where the kinetic energy exceeds the potential energy can still form bound clusters, although at a smaller efficiency. For an assumed SFE of 0.25 and a gas dispersal time of 1 Myr, or two crossing times, Baumgardt & Kroupa (2007) estimated that roughly 55% of the stars may remain bound. Note that Baumgardt & Kroupa (2007) assumed the radial density profiles of the stars and of the residual gas in an embedded cluster have the same shape. If the density profile of the stars is steeper than the profile of the gas, which is likely for the inner regions, then the likelihood of the formation of a bound cluster increases substantially (see Adams 2000; Parmentier & Pfalzner 2013; Shukirgaliyev et al. 2017).

A key parameter is $T/|U|$, known as the virial ratio (Q). Farias et al. (2018), “based on the value of Q just after gas dispersal,” estimated the fraction of stars that remains bound after gas dispersal. They compared simple models and simulations to show that the bound number strongly depends on the initial post-gas-dispersal virial ratio. We expect the value of $T/|U|$ to slowly increase as the cluster expands. For a binary fraction of 0.5, the expectation value of the velocity dispersion for $\log(T/|U|) \sim 0.3$; for this value of Q , $\sim 35\%$ of the stars will remain bound. At the 25th percentile, the $\log(T/|U|)$ value is 0.1, which corresponds to 55% of the members remaining bound and at the 75th percentile, the $\log(T/|U|)$ value is 0.76, which corresponds to 10% of the members remaining bound. If the velocity dispersion is closer to those inferred for a binary fraction of 0, then 10% or less will remain bound. If the binary fraction is 1, then up to 95% of the members remain bound in the 25th percentile and as few as 20% members will remain bound in the 75th percentile. Kuhn et al. (2018) found a velocity dispersion of $1.9 \pm 0.2 \text{ km s}^{-1}$ and that the cluster is expanding radially. This is similar to the expectation value with a velocity dispersion of 2.2 km s^{-1} for a binary fraction of 0.5, which is the binary fraction that is most consistent with that of solar-type stars (Duchêne & Kraus 2013). Although a broad range of outcomes are allowed, we favor where approximately a third of the stars remain bound.

5.2. The Possible Early Conditions and Evolutionary Paths of the Western Subcluster

The smaller western subcluster remains more embedded than the eastern subcluster. We calculate a current SFE between 0.23 and 0.26 depending on the disk fraction, which is much higher than the eastern subcluster. Even though it is similar to SFEs of embedded clusters, the gas is offset to the south of the center of the subcluster, which appears to have at least partially dispersed its gas (Allen et al. 2012). Additional evidence that it is not as dynamically evolved as the eastern subcluster is its elongated morphology and smaller core size (0.5 ± 0.3 pc).

The lesser degree of dynamical evolution in the west does not necessarily imply a younger age. The west contains one B3 and three B5 stars that do not have the UV radiation of the O7 star in the eastern subcluster to clear natal gas as quickly. Calculating a crossing time as in Section 5.1 yields $t_{\text{crossing}} = 1.45 \pm 0.31$ Myr. The west has experienced ~ 3 crossings since the formation of the cluster, similar to the eastern subcluster, assuming an age of 3–4 Myr. The relaxation time is ~ 19 –22 Myr for the two disk fractions. This indicates the west is not dynamically relaxed and could maintain its elongated morphology. The core radius is larger than that of the ONC and NGC 2024 (see Section 5.1), and the surface densities (220 and 182 stars pc^{-2}) are lower suggesting that the core of the subcluster has expanded.

As the western subcluster evolves, it is unclear how quickly the remaining natal gas will disperse and how the virial ratio will change as a result. It is a reasonable assumption that $T/|U|$ will increase as it expands, but by how much remains unclear. Our range of $\log(T/|U|)$ values (Figure 11) is consistent with a cluster that is currently virialized, although with large error bars.

If this virial ratio is maintained through gas dispersal, then we can again compare our $\log(T/|U|)$ values to Figure 7 in Farias et al. (2018) to determine the fraction of stars that will remain bound as in Section 5.1. For a binary fraction of 0.5, the expectation value of $\log(T/|U|)$ is -0.16 , which yields $\sim 75\%$ of the stars remaining bound. At the 25th and the 75th percentiles, the $\log(T/|U|)$ value is -0.5 and 0.47 , which corresponds to 98% and 20% of members remaining bound, respectively. If the velocity dispersion is closer to those inferred for a binary fraction of 0, then the expectation value of $\log(T/|U|)$ is 0.27, resulting in 30% of the stars remaining bound. For the 25th and 75th percentiles, as many as 50% and as few as 10% of the members will remain bound, respectively. If the binary fraction is 1, the expectation value results in 95% of the stars remaining bound. If we take the 25th and 75th percentiles, the number of remaining members will be 100% and 30%, respectively. Although a broad range of outcomes is allowed, we favor where approximately 75% of the stars remain bound. Baumgardt & Kroupa (2007) found that a combination of very slow gas expulsion and a very weak external tidal field with an initial SFE of 33% can produce a bound cluster with 90% of stars remaining bound. The current SFE is 26%, and it is possible that the west initially had an SFE of $\sim 30\%$. If the timescale of gas dispersal is prolonged, which is the likely case in the west, then the fraction of bound stars may be higher (Baumgardt & Kroupa 2007).

5.3. Fate of Cep OB3b

Our values for the virial ratios are consistent with Cep OB3b forming two bound subclusters, each with ~ 300 stars. These two subclusters would be found within an expanding association of stars from the lower density halo surrounding both of the subclusters, as well as the members ejected from the subclusters. The associations would have more stars than the clusters combined.

To determine whether the two subclusters may merge into a single cluster, we compare the escape velocity to the relative motions of the two subclusters. The escape velocity is $v_{\text{esc}} = (2GM_{\text{tot}}/R)$, where M_{tot} is the combined stellar mass of the east and west. We use the most optimistic masses of stars, i.e., $(809 + 501) \times 0.5 M_{\odot}$ and a separation of the subclusters of 5 pc as R . This results in an escape velocity of 1.06 km s^{-1} . The total proper motion of Cep OB3b is subtracted off the proper motions of the subclusters. The east is moving at -0.47 km s^{-1} , and the west is moving at 1.55 km s^{-1} for a difference in 2.02 km s^{-1} . Considering that the masses of the subclusters will be lower after gas dispersal and that the actual separation is likely to be larger than the projected separation, this escape velocity should be considered as an upper limit. Thus, the two subclusters are moving away from each other at a velocity that exceeds the escape velocity and will only increase in separation, forming a double cluster.

This result seems exceptional in light of the fact that $\sim 7\%$ of embedded clusters form open clusters (Lada & Lada 2003). This might be due to unusual conditions in the Cep OB3b cluster. Alternatively, there might be other factors that contribute to the dissipation of clusters (see Moeckel et al. 2012), particularly when a realistic range of masses is used. Stellar dynamical effects come into play when binaries and a realistic range of masses are used (Moeckel et al. 2012). Alternatively, the tidal forces between the clusters, and between the clusters and the molecular clouds, may disrupt the clusters or strip members. It should also be noted that the large uncertainties in the velocity dispersions translate into large uncertainties in the dynamical outcomes. If both subclusters form bound clusters, then the study of Cep OB3b will help establish the cluster properties and environmental factors that produce bound clusters.

5.4. The Effect of Binarity on the Velocity Dispersions of Young Clusters

One of the results of our analysis is that the adopted binary fraction strongly influences the PDFs for the cluster velocity dispersions, as demonstrated in Figure 8. This importance can be further demonstrated by a simple comparison of the expected velocity dispersion due to binarity compared to that from clusters. We compare these by approximating the ratio of the velocity dispersion from cluster motions to that from binary motions.

The 1D velocity dispersion of a barely bound ($U = T$) cluster is given by

$$\sigma_{\text{1D}}^2 = \alpha \frac{GM}{R}, \quad (4)$$

where M is the total mass of the cluster, R is the core radius of the cluster, and α depends on the radial density distribution of the spherically symmetric cluster. We adopt the value of $\alpha = 2/5$, which is that for a uniform density cluster. For a

cluster, the observed velocity dispersion due to the motions of binaries is approximately

$$\sigma_{\text{bin}}^2 = f_{\text{bin}} \beta \frac{Gm}{r}, \quad (5)$$

where m is the combined mass of the system, r is the typical semimajor axis, f_{bin} is the binary fraction, and β takes into account the effect of orbital inclinations and orbital phases on the line-of-sight velocity. The 0.5 term assumes that the reduced mass is half the combined mass. We adopt $\beta = 2/3$, $m = 1.5 M_{\odot}$, and a semimajor axis of 45 au; this is the peak of the log-normal semimajor axis distribution for solar-mass field stars (Duchêne & Kraus 2013). Throughout the following analysis, we assume $f_{\text{bin}} = 0.5$. The adopted system mass of $1.5 M_{\odot}$ assumes that the stars with measured velocity dispersions have masses of $0.75 M_{\odot}$ each.

To compare the magnitudes of the binary motions and motions within a cluster, we consider the ratio of the two velocities dispersions, which is given by

$$\frac{\sigma_{\text{bin}}^2}{\sigma_{\text{ID}}^2} = f_{\text{bin}} \left(\frac{\beta}{\alpha} \right) \left(\frac{m_{\text{bin}}}{N_* m_*} \right) \left(\frac{R}{r} \right), \quad (6)$$

where N_* is the total number of stellar systems (including single and multiple stars) in the cluster and m_* is the average mass of the cluster members. The adopted mass of the cluster members is $m_* = 0.75(1 + f_{\text{bin}}) M_{\odot}$, where the average mass of an individual star with a measured velocity is assumed to be $0.75 M_{\odot}$. For a cluster with $N_* = 500$, we find that for the ratio of velocity dispersions to be equal to or less than 1 (i.e., that the cluster motions are equal to or exceed those of the binaries), the cluster radius must be ≤ 0.1 pc. This ratio increases linearly with the number of stars. Thus, for all but the youngest, most compact clusters, the motions of the binaries dominate the observed velocity dispersion.

For embedded clusters, the dominant mass is that of the molecular gas. This requires us to include the SFE in Equation (6); the SFE is the ratio of the mass in stars over the combined stellar and gas mass. Specifically, the value of $N_* m_*$ must be replaced with $N_* m_*/\text{SFE}$. If we adopt $\text{SFE} = 0.2$, a common value for young clusters at earlier phases of gas dispersal (e.g., Megeath et al. 2016), then the velocity dispersion ratio is unity or less for $R \leq 0.5$ pc. Thus, in the case of young embedded clusters, which have typical radii of 0.5 pc, the contribution of cluster motions can exceed or equal those from binaries due to the effect of the gas mass on the cluster motions. As the gas is dispersed and the cluster expands, binaries will begin to dominate the observed distribution if it remains in virial equilibrium while expanding.

6. Summary

We present a study of the spatial structure and kinematics of Cep OB3b, a young cluster currently in a late stage of gas dispersal. Cep OB3b is one of the closest examples of a ~ 3 –5 Myr, large (~ 3000 total members) cluster. The cluster is broken into two subclusters: the east, which contains an O7 star, and west, which has several B stars. Using the combined sample of members identified with IR excesses or X-ray detections (Allen et al. 2012), the structure, density structures, and deviation from circular symmetry of the two subclusters

are determined from fitting the empirical density law of King (1962). We present new RV measurements from Hectoschelle of 499 stars; 109 of these are likely confirmed members of Cep OB3b with youth indicators. After excluding potential binaries and applying an R cut, 3σ clipping, and subcluster radius cut to the data, we are left with 52 stars in our RV analysis.

1. We derive the distance to Cep OB3b using known members found in the *Gaia* DR2 catalog. The distance is 819 ± 16 pc.
2. Fits to the empirical King (1962) models yield the properties of the cluster. For the eastern subcluster, we find a core radius of 1.36 ± 0.30 pc and a peak density of 428 – 521 stars pc^{-2} , depending on the adopted disk fraction. For the western subcluster, we find a core radius of 0.52 ± 0.11 pc and a peak density of 284 and 342 stars pc^{-2} . The subcluster radii of the subclusters are 2.32 ± 0.19 pc in the east, with 664–809 stars within this border, and 3.1 ± 1.0 pc in the west, with 332–402 stars within this border.
3. We have determined the posterior probability distribution for the velocity dispersion of each subcluster. This analysis includes a contribution due to binaries for an assumed binary fraction. The peaks of the distributions in the east are $2.8_{-0.7}^{+0.6}$ km s^{-1} , 2.2 ± 1.0 km s^{-1} , and $1.15_{-0.95}^{+0.80}$ km s^{-1} for a binary fractions of 0, 0.5, and 1, respectively. The expectation values are $2.8_{-0.7}^{+0.6}$ km s^{-1} , 1.9 ± 1.0 km s^{-1} , and $1.4_{-1.0}^{+0.8}$ km s^{-1} for binary fractions of 0, 0.5, and 1, respectively. The west has velocity dispersion peaks at $1.5_{-0.3}^{+0.70}$ km s^{-1} , $0.5_{-0.5}^{+0.8}$ km s^{-1} , and $0.3_{-0.3}^{+0.6}$ km s^{-1} with expectation values of $1.5_{-0.50}^{+0.70}$ km s^{-1} , $1.1_{-0.5}^{+0.8}$ km s^{-1} , and $1.0_{-0.3}^{+0.6}$ km s^{-1} for binary fractions of 0, 0.5, and 1, respectively. Using *Gaia* DR2 proper motions, Kuhn et al. (2018) found a velocity dispersion of 1.9 ± 0.2 km s^{-1} for the east.
4. A comparison of the eastern subcluster with the NGC 2024 and ONC cluster indicates that this cluster has a much larger core radius and lower central density. It also is circularly symmetric. This is evidence that this cluster has undergone significant expansion. Although the western subcluster is more compact than the eastern one and shows a significant asymmetry, it still has a larger core radius and lower central density than the two Orion clusters. This subcluster also appears to have undergone some degree of expansion.
5. The inferred ratio of the kinetic to potential energy of the eastern subcluster, $T/|U|$, shows that this ratio depends strongly on the adopted binary fraction for the stars. For a binary fraction of 0 and 0.5, $\log(T/|U|) > 0$, suggesting the subcluster will undergo expansion. For a binary fraction of 1, which is unlikely, there is a moderate probability that the cluster could be bound. We conclude that this subcluster most likely has a ratio greater than 1 and is expanding.
6. A similar analysis for the western subcluster shows $\log(T/|U|) \sim 0$ for binary fractions of 0.5 and 1, but $\log(T/|U|) > 0$ for a binary fraction of 0. We conclude that this subcluster is close to bound and may be virialized.
7. Accounting for unresolved binaries is important to accurately probe the dynamical properties of young clusters, particularly after gas dispersal. The binary motions can dominate the motions of the cluster, and

this is particularly important when limited to solar-mass stars with a high fraction of multiplicity.

8. For the binary fraction of 0.5, we find that the eastern subcluster is more likely in a state of expansion. Comparisons to nbody simulations suggest that 35% of the member stars may remain to form a bound cluster. In contrast, the western subcluster may be near virial equilibrium where close to 75% of the members remain bound. These two different outcomes may be driven by the rapid dispersal of gas in the eastern subcluster, due to the presence of an O7 star. In contrast, the western subcluster, which still contains a significant mass of gas, only contains massive stars of spectral type B3 or later.
9. A likely outcome is that the two subclusters will form bound clusters with 300 stars. An analysis of the bulk proper motion of the two subclusters using *Gaia* DR2 shows that the subclusters are moving away from each other with $\sim 2 \text{ km s}^{-1}$, and they are not bound. Thus, Cep OB3b may be forming two, independent bound clusters. Given that only $\sim 7\%$ of embedded clusters survive to form bound clusters, this is a very rare outcome, suggesting that the physical conditions in Cep OB3b are highly conducive to bound cluster formation. Alternatively, other factors that have been ignored in our analysis, such as internal dynamics of clusters or tidal forces, may play an important role in the disruption of clusters; if this is the case, the nascent bound clusters in Cep OB3b may still be disrupted.

We wish to thank the anonymous referee for excellent suggestions that improved the quality of this manuscript. The authors are also grateful to M. Kounkel for useful discussions and comments throughout the progress of this project. This work was supported by NSF grant AST-1009564 to S.T.M. R. A.G. gratefully acknowledges funding support from NASA ADAP grants NNX11AD14G, NNX15AF05G, and NNX17AF24G; NASA JPL/Caltech contract 1489384; and NSF grant AST 1636621 in support of TolTEC, the next generation mm-wave camera for LMT. Data presented herein were obtained at the MMT Observatory at Fred Lawrence Whipple Observatory on Mount Hopkins, AZ, USA. This work made use of the SIMBAD database, the VizieR database, the NASA Astrophysics Data System, and the data products from the Two Micron All Sky Survey, which is a joint project of the University of Massachusetts and the Infrared Processing and Analysis Center/California Institute of Technology, funded by the National Aeronautics and Space Administration and the NSF.

This work has made use of data from the European Space Agency (ESA) mission *Gaia* (<https://www.cosmos.esa.int/gaia>), processed by the *Gaia* Data Processing and Analysis Consortium (DPAC, <https://www.cosmos.esa.int/web/gaia/dpac/consortium>). Funding for the DPAC has been provided by national institutions, in particular the institutions participating in the *Gaia* Multilateral Agreement.

Appendix Calcium II H & K Emission

Ca II H and K line emission is an indicator of youth and a way of identifying diskless pre-MS stars that do not have detectable X-ray emission. Emission in the H&K lines (3968.5 Å and 3933.7 Å, respectively) in a spectrum may

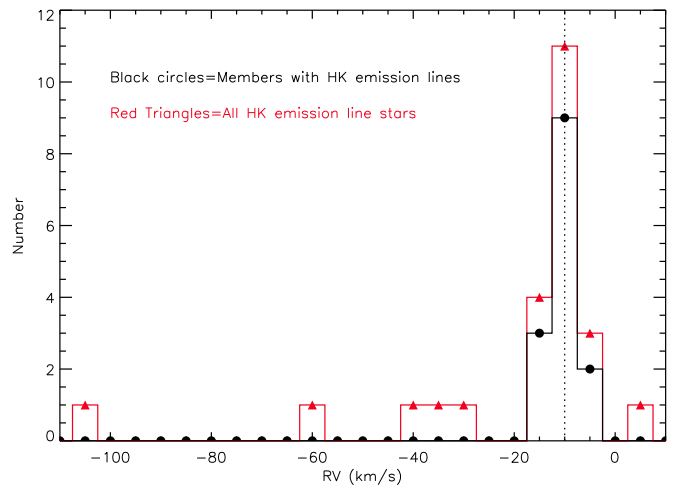


Figure 15. Histogram of RVs of stars marked with HK emission lines and RV values larger than 5.0. The histograms marked by the black circles are for objects with youth indicators, and the red triangles are for all objects with H&K emission lines. There is a clear peak of the objects with youth indicators at -10 km s^{-1} (dotted line) that corresponds to the V_{lsr} peak of Cep OB3b.

indicate magnetic activity in the chromosphere. As stars contract onto the main sequence, their magnetic fields can be stronger than when they reach the main sequence. The increased magnetic field may be due to rapid rotation of stars in the pre-MS phase (Johns-Krull et al. 1999). We used the Hectospec data to determine if any of our objects had H&K emission. When we observed emission in the line core, the object was marked to have H&K emission. Fifteen objects with Ca II H&K line emission in our sample had no previous indications of youth as well as 25 objects that had at least one youth indicator already.

As seen in Figure 15, most (83%) objects with H&K emission have RVs within 3σ of the average RV of the cluster, whereas 46% of the objects without youth indicators are within 3σ of the average RV of the cluster. The outliers with H&K emission may be binaries that we simply have not detected or may indicate that $\sim 20\%$ of the objects identified by H&K emission may be contaminants.

ORCID iDs

J. J. Prchlik <https://orcid.org/0000-0002-3517-9421>
 R. A. Gutermuth <https://orcid.org/0000-0002-6447-899X>
 S. T. Megeath <https://orcid.org/0000-0001-7629-3573>
 J. L. Pipher <https://orcid.org/0000-0002-0628-9605>
 S. Wolk <https://orcid.org/0000-0002-0826-9261>

References

- Adams, F. C. 2000, *ApJ*, 542, 964
 Adams, J. D., Stauffer, J. R., Monet, D. G., Skrutskie, M. F., & Beichman, C. A. 2001, *AJ*, 121, 2053
 Allen, L., Megeath, S. T., Gutermuth, R., et al. 2007, in *Protostars and Planets V* (Tucson: University of Arizona Press), 361
 Allen, T. S., Gutermuth, R. A., Kryukova, E., et al. 2012, *ApJ*, 750, 125
 Allen, T. S., Prchlik, J. J., Megeath, S. T., et al. 2014, *ApJ*, 786, 113
 Baumgardt, H., & Kroupa, P. 2007, *MNRAS*, 380, 1589
 Blaauw, A., Hiltner, W. A., & Johnson, H. L. 1959, *ApJ*, 130, 69
 Boily, C. M., & Kroupa, P. 2003, *MNRAS*, 338, 673
 Carpenter, J. M. 2000, *AJ*, 120, 3139
 Chen, H.-C., & Ko, C.-M. 2009, *ApJ*, 698, 1659
 Coelho, P., Barbuy, B., Meléndez, J., Schiavon, R. P., & Castilho, B. V. 2005, *A&A*, 443, 735

- Cottaar, M., Covey, K. R., Foster, J. B., et al. 2015, *ApJ*, **807**, 27
- Cottaar, M., Meyer, M. R., & Parker, R. J. 2012, *A&A*, **547**, A35
- Dahm, S. E., & Simon, T. 2005, *AJ*, **129**, 829
- Da Rio, N., Tan, J. C., Covey, K. R., et al. 2017, *ApJ*, **845**, 105
- Da Rio, N., Tan, J. C., & Jachnig, K. 2014, *ApJ*, **795**, 55
- Duchêne, G., & Kraus, A. 2013, *ARA&A*, **51**, 269
- Evans, N. J., II, Dunham, M. M., Jørgensen, J. K., et al. 2009, *ApJS*, **181**, 321
- Farias, J. P., Fellhauer, M., Smith, R., Domínguez, R., & Dabringhausen, J. 2018, *MNRAS*, **476**, 5341
- Farias, J. P., Smith, R., Fellhauer, M., et al. 2015, *MNRAS*, **450**, 2451
- Foster, J. B., Cottaar, M., Covey, K. R., et al. 2015, *ApJ*, **799**, 136
- Fűrész, G., Hartmann, L. W., Megeath, S. T., Szentgyorgyi, A. H., & Hamden, E. T. 2008, *ApJ*, **676**, 1109
- Fűrész, G., Hartmann, L. W., Szentgyorgyi, A. H., et al. 2006, *ApJ*, **648**, 1090
- Getman, K. V., Feigelson, E. D., Luhman, K. L., et al. 2009, *ApJ*, **699**, 1454
- Geyer, M. P., & Burkert, A. 2001, *MNRAS*, **323**, 988
- Goodwin, S. P. 2009, *Ap&SS*, **324**, 259
- Gutermuth, R. A., Allen, T., Megeath, T., Pipher, J., & Wolk, S. 2011a, AAS Meeting Abstracts, **43**, 258.19
- Gutermuth, R. A., Megeath, S. T., Myers, P. C., et al. 2009, *ApJS*, **184**, 18
- Gutermuth, R. A., Megeath, S. T., Pipher, J. L., et al. 2005, *ApJ*, **632**, 397
- Gutermuth, R. A., Pipher, J. L., Megeath, S. T., et al. 2011b, *ApJ*, **739**, 84
- Heyer, M. H., Carpenter, J. M., & Ladd, E. F. 1996, *ApJ*, **463**, 630
- Hillenbrand, L. A., & Hartmann, L. W. 1998, *ApJ*, **492**, 540
- Jeffries, R. D., Jackson, R. J., Cottaar, M., et al. 2014, *A&A*, **563**, A94
- Jeffries, R. D., Maxted, P. F. L., Oliveira, J. M., & Naylor, T. 2006, *MNRAS*, **371**, L6
- Johns-Krull, C. M., Valenti, J. A., Hatzes, A. P., & Kanaan, A. 1999, *ApJL*, **510**, L41
- King, I. 1962, *AJ*, **67**, 471
- Kounkel, M., Hartmann, L., Mateo, M., & Bailey, J. I., III 2017, *ApJ*, **844**, 138
- Kounkel, M., Hartmann, L., Tobin, J. J., et al. 2016, *ApJ*, **821**, 8
- Kuhn, M. A., Feigelson, E. D., Getman, K. V., et al. 2014, *ApJ*, **787**, 107
- Kuhn, M. A., Hillenbrand, L. A., Sills, A., Feigelson, E. D., & Getman, K. V. 2018, arXiv:1807.02115
- Kurtz, M. J., & Mink, D. J. 1998, *PASP*, **110**, 934
- Kurucz, R. L. 1993, *PhST*, **47**, 110
- Lada, C. J., & Lada, E. A. 2003, *ARA&A*, **41**, 57
- Lada, C. J., Margulis, M., & Dearborn, D. 1984, *ApJ*, **285**, 141
- Lindgren, L., Hernández, J., Bombrun, A., et al. 2018, *A&A*, **616**, A2
- Littlefair, S. P., Naylor, T., Mayne, N. J., Saunders, E. S., & Jeffries, R. D. 2010, *MNRAS*, **403**, 545
- MacLaren, I., Richardson, K. M., & Wolfendale, A. W. 1988, *ApJ*, **333**, 821
- Markwardt, C. B. 2009, in ASP Conf. Ser. 411, *Astronomical Data Analysis Software and Systems XVIII*, ed. D. A. Bohlender, D. Durand, & P. Dowler (San Francisco, CA: ASP), 251
- Marrese, P. M., Marinoni, S., Fabrizio, M., & Altavilla, G. 2018, arXiv:1808.09151
- Mayne, N. J., Naylor, T., Littlefair, S. P., Saunders, E. S., & Jeffries, R. D. 2007, *MNRAS*, **375**, 1220
- Megeath, S. T., Gutermuth, R., Muzerolle, J., et al. 2016, *AJ*, **151**, 5
- Moeckel, N., & Bate, M. R. 2010, *MNRAS*, **404**, 721
- Moeckel, N., Holland, C., Clarke, C. J., & Bonnell, I. A. 2012, *MNRAS*, **425**, 450
- Moscadelli, L., Reid, M. J., Menten, K. M., et al. 2009, *ApJ*, **693**, 406
- Munari, U., Sordo, R., Castelli, F., & Zwitter, T. 2005, *A&A*, **442**, 1127
- Ortiz-León, G. N., Loinard, L., & Dzib, S. A. 2018, arXiv:1812.02360
- Parmentier, G., & Pfalzner, S. 2013, *A&A*, **549**, A132
- Pelupessy, F. I., & Portegies Zwart, S. 2012, *MNRAS*, **420**, 1503
- Proszkow, E.-M., Adams, F. C., Hartmann, L. W., & Tobin, J. J. 2009, *ApJ*, **697**, 1020
- Rapson, V. A., Pipher, J. L., Gutermuth, R., et al. 2014, *ApJ*, **794**, 124
- Rigliaco, E., Wilking, B., Meyer, M. R., et al. 2016, *A&A*, **588**, A123
- Sacco, G. G., Spina, L., Randich, S., et al. 2017, *A&A*, **601**, A97
- Sargent, A. I. 1977, *ApJ*, **218**, 736
- Shukirgaliyev, B., Parmentier, G., Berczik, P., & Just, A. 2017, *A&A*, **605**, A119
- Sicilia-Aguilar, A., Hartmann, L. W., Szentgyorgyi, A. H., et al. 2005, *AJ*, **129**, 363
- Szentgyorgyi, A. 2006, *NewAR*, **50**, 326
- Szentgyorgyi, A. H., Cheimets, P., Eng, R., et al. 1998, *Proc. SPIE*, **3355**, 242
- Tobin, J. J., Hartmann, L., Fűrész, G., Hsu, W.-H., & Mateo, M. 2015, *AJ*, **149**, 119
- Tobin, J. J., Hartmann, L., Fűrész, G., Mateo, M., & Megeath, S. T. 2009, *ApJ*, **697**, 1103
- Tonry, J., & Davis, M. 1979, *AJ*, **84**, 1511